

2009

## Novel optical components for non-mechanical beam steering

Katherine Lisa Drain  
*University of Dayton*

Follow this and additional works at: [https://ecommons.udayton.edu/graduate\\_theses](https://ecommons.udayton.edu/graduate_theses)

---

### Recommended Citation

Drain, Katherine Lisa, "Novel optical components for non-mechanical beam steering" (2009). *Graduate Theses and Dissertations*. 2422.  
[https://ecommons.udayton.edu/graduate\\_theses/2422](https://ecommons.udayton.edu/graduate_theses/2422)

This Thesis is brought to you for free and open access by the Theses and Dissertations at eCommons. It has been accepted for inclusion in Graduate Theses and Dissertations by an authorized administrator of eCommons. For more information, please contact [mschlange1@udayton.edu](mailto:mschlange1@udayton.edu), [ecommons@udayton.edu](mailto:ecommons@udayton.edu).

**NOVEL OPTICAL COMPONENTS FOR NON-MECHANICAL BEAM  
STEERING**

Thesis

Submitted to

The School of Engineering of the  
UNIVERSITY OF DAYTON

In Partial Fulfillment of the Requirements for

The Degree

Master of Science in Electro-Optics

by

Katherine Lisa Drain

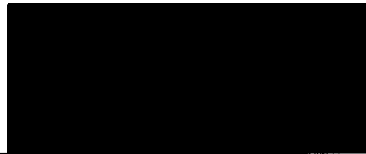
UNIVERSITY OF DAYTON

Dayton, Ohio

August 2009

# NOVEL OPTICAL COMPONENTS FOR NON-MECHANICAL BEAM STEERING

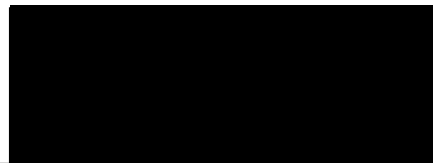
APPROVED BY:



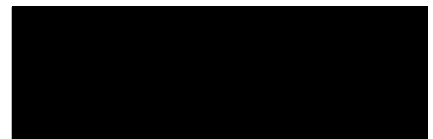
Qiwen Zhan, Ph.D.  
Advisory Committee Chairman  
Associate Professor  
Electro-Optics Program



Robert L. Nelson, Ph.D.  
Committee Member  
Research Physicist  
AFRL/RXPSO, WPAFB, OH



Joseph W. Haus, Ph.D.  
Committee Member  
Professor & Director  
Electro-Optics Program



Edward A. Watson, Ph.D.  
Committee Member  
Research Advisor  
ARFL/RYPJ, WPAFB, OH



Malcolm W. Daniels, Ph.D.  
Associate Dean for Graduate Studies  
School of Engineering



Joseph E. Saliba, Ph.D., P.E.  
Dean  
School of Engineering

## ABSTRACT

### NOVEL OPTICAL COMPONENTS FOR NON-MECHANICAL BEAM STEERING

Name: Drain, Katherine L.  
University of Dayton, August 2009

Advisor: Dr. Qiwen Zhan

Non-mechanical beam steering can be accomplished by various devices/techniques such as a liquid crystal spatial light modulator or a parabolic mirror combined with a Goos-Hänchen focal plane shifter. For this application, a suitable transmit/receive (Tx/Rx) switch that isolates the transmitter from the receiver of the system is required. For a liquid crystal spatial light modulator, beam steering occurs when the incident beam is linearly polarized at a prescribed orientation. Previous Tx/Rx switches utilized a circularly polarized beam in conjunction with a polarization beam splitter, which proved to be a lossy solution. By using a two-dimensional reflection type liquid crystal spatial light modulator with a large aperture Faraday rotator, it is possible to develop a more efficient Tx/Rx switch for non-mechanical beam steering, which can be applied to laser scanning imaging systems. In the first section of this thesis, I will present the proposed design of such a switch along with demonstrating the experimental results at a  $1.064\mu\text{m}$  operation wavelength for steering angles up to about  $2^\circ$ . Also, the characterization of the Faraday rotator was addressed in terms of its allowable field of view and imaging quality.

For the second portion of this thesis, electronic electro-optic beam steering techniques will be discussed for faster scanning speeds, larger steering angles, and higher efficiency

than liquid crystal spatial light modulators. In particular, calculations for the theoretical and experimental steering angles at various translational distances of a parabolic mirror are shown. Finally, the theory behind utilizing the Goos-Hänchen effect as a focal plane shifter will be presented.

## ACKNOWLEDGMENTS

I would first like to extend special thanks to my advisor Qiwen Zhan for all of his assistance and support throughout the course of my research. I would also like to thank all of my professors who introduced me to the world of optics as well as all of my fellow classmates who helped me approach problems from different viewpoints. Finally, I would like to thank the Sensors Directorate of the Air Force Research Lab at Wright Patterson Air Force Base and the University of Dayton Ladar and Optical Communications Institute (LOCI) for funding my pursuit of a Master's degree in electro-optics.

# TABLE OF CONTENTS

ABSTRACT.....	ii
ACKNOWLEDGMENTS .....	iv
LIST OF ILLUSTRATIONS .....	vii
LIST OF TABLES .....	ix
CHAPTER I: INTRODUCTION.....	1
1.1 Spatial Light Modulator.....	1
1.2 Beam Steering.....	2
1.2.1 Mechanical Techniques .....	3
1.2.2 Non-mechanical Techniques .....	3
CHAPTER II: BEAM STEERING WITH LC-SLM .....	6
2.1 Principle .....	6
2.2 Modeling of Beam Steering with LC-SLM .....	10
2.2.1 Analytical Model .....	12
2.2.2 Numerical Model .....	15
2.3 Polarization Issues .....	18
CHAPTER III: EFFICIENT TRANSMIT/RECEIVE SWITCH .....	19
3.1 Design and Principle .....	19
3.1.1 Design Schematic .....	20
3.1.2 Polarization Study via Jones Calculus.....	22
3.1.3 Polarization Study via Schematic .....	25
3.2 Experimental Verification.....	26
3.2.1 Discussions .....	35
3.3 Imaging Capabilities .....	36
CHAPTER IV: ELECTRONIC ELECTRO-OPTIC BEAM STEERING .....	38
4.1 Why Electronic Electro-Optic Beam Steering.....	38
4.2 Gaussian Beam Optics of Parabolic Mirror .....	40
4.2.1 Setting Parameters for Experiment.....	45
4.2.2 Gaussian Beam Profile .....	49
4.2.3 Steering Angle Calculation.....	53
4.3 Goos-Hänchen Shifter.....	57
4.3.1 Theory.....	58

4.3.2 Numerical Simulation.....	62
CHAPTER V: CONCLUSIONS AND FUTURE WORK.....	66
APPENDIX A.....	70
A.1 MatLab Code for Generating the Analytical Model in Chapter 2 .....	70
A.2 MatLab Code for Generating the Numerical Model in Chapter 2 .....	72
A.2.1 MatLab Code for Figure 2.6 .....	72
A.2.2 MatLab Code for Figure 2.7 .....	74
APPENDIX B .....	77
B.1 MatLab Code for Generating Figures in Chapter 4.....	77
B.1.1 MatLab Code for Figure 4.5 .....	77
B.1.2 MatLab Code for Figure 4.9 .....	80
B.1.3 MatLab Code for Figures 4.13 and 4.14 .....	80
REFERENCES .....	84



## LIST OF ILLUSTRATIONS

Figure 1.1 Boulder Nonlinear Systems LC-SLM .....	4
Figure 1.2 Schematic of a blazed grating.....	5
Figure 1.3 Schematic showing the flyback region.....	5
Figure 2.1 Cross-sectional illustration of LC-SLM.....	6
Figure 2.2 Illustration of $2\pi$ phase reset of blazed grating .....	9
Figure 2.3 Illustration of BNS LC-SLM.....	10
Figure 2.4 Analytical model for a steering angle of about $2^\circ$ .....	14
Figure 2.5 Analytical model for steering angles of about $0.5^\circ$ , $1^\circ$ , and $2^\circ$ .....	15
Figure 2.6 Numerical model for a steering angle of about $2^\circ$ .....	16
Figure 2.7 Numerical model for steering angles of about $0.5^\circ$ , $1^\circ$ , and $2^\circ$ .....	17
Figure 3.1 Schematic of the Tx/Rx switch design .....	20
Figure 3.2 Schematic showing polarization states.....	26
Figure 3.3 Experimental setup .....	27
Figure 3.4 Schematic for power measurements of Tx/Rx switch.....	29
Figure 3.5 Image of entire beam (left) and of the edge of the mirror (right).....	37
Figure 4.1 Block diagram representation for EO beam steering .....	41
Figure 4.2 Reflection of a beam on a parabolic surface .....	42
Figure 4.3 Schematic for beam steering with a $30^\circ$ offset parabolic mirror.....	46
Figure 4.4 Experimental setup for beam profiling.....	49
Figure 4.5 Gaussian beam profile of parabolic mirror.....	51
Figure 4.6 Image of beam at a distance, $z_{\text{off}}$ , from the mirror.....	52
Figure 4.7 Image of beam at a distance of $\sim 39$ inches from the mirror.....	53

Figure 4.8 Illustration of an off-axis parabolic mirror .....	54
Figure 4.9 Plot of theoretical and experimental steering angles vs. mirror translation ....	57
Figure 4.10 Illustration of Goos-Hänchen effect .....	59
Figure 4.11 Illustration of Goos-Hänchen shift in a waveguide .....	60
Figure 4.12 Illustration of Goos-Hänchen shifter .....	61
Figure 4.13 Plots showing both the absolute and normalized beam profile versus transverse distance .....	63
Figure 4.14 Plots showing the resonances of the various modes (top) and the phase (bottom) of the reflected beams versus the incident angle .....	64

## LIST OF TABLES

Table 2.1 Ideal 1st order diffraction efficiency as a function of the # of phase levels .....	8
Table 2.2 Theoretical steering angle based on number of pixels per grating period .....	11
Table 3.1 Power measurements for mirror in place of LC-SLM .....	29
Table 3.2 Power measurements for $2.0325^\circ$ steering angle .....	32
Table 3.3 Power measurements for $1.0161^\circ$ steering angle .....	34
Table 4.1 Theoretical steering angle calculation in terms of the mirror translation .....	55
Table 4.2 Experimental steering angle calculation in terms of the translation of the spot at a distance of 1080mm .....	56

## CHAPTER I: INTRODUCTION

### 1.1 Spatial Light Modulator

A spatial light modulator (SLM) is a device that spatially modulates the properties of light based on a fixed pixel pattern. Across the area of this pixel pattern, the amplitude and/or phase can be electronically controlled [1]. This relates to digitized data being changed into coherent optical information that can be used in such applications as beam steering, optical tweezers, wave front correction, and diffractive optics to name a few [2]. There are two types of SLMs – electrically addressed and optically addressed. Electrically addressed SLMs (EASLMs) and optically addressed SLMs (OASLMs) change data from electrical and incoherent optical signals into spatially modulated coherent optical signals, respectively. OASLMs possess a number of attractive characteristics that are of particular value for optical processing systems. These characteristics include fast temporal response, the conversion of images from incoherent to coherent, image amplification, and wavelength conversion [3].

As mentioned above, SLMs are primarily used to process data that is inputted; however, they can also be used to produce spatial filters that can be adjusted in real time. Since the beginning of optical information processing, a number of various SLM devices have been devised, which include most importantly liquid crystal (LC) SLMs, magneto-optic (MO) SLMs, deformable mirror SLMs, multiple-quantum-well (MQW) SLMs, and acousto-optic (AO) Bragg cells [3]. Of these devices, the LC-SLM is discussed in further detail

in the next chapter since it is present in the proposed efficient transmit/receive (Tx/Rx) switch design.

## 1.2 Beam Steering

Beam steering, or light deflection, has become an integral part of free space optical communications (FSOC) and laser radar (LADAR) systems in such areas as imaging and tracking of targets. Generally, it is done by causing a lag in the phase profile of the laser beam [4]. In simpler terms, beam steering involves shifting the angle of the main lobe of a beam in order to position it at a desired location. The ability to control where a beam is positioned is an important aspect in applications relating to telecommunications, national defense, and industry.

There are two main beam steering techniques – mechanical and non-mechanical beam steering. Perhaps the most commonly used beam steering device in optics is a large mechanically controllable mirror. Unfortunately, such an approach possesses a major limitation with the mechanical movement of the mirror, thus affecting the overall steering speed [5]. There is also the issue that a relatively large aperture is needed for steering a small beam, which is related to the Lagrange invariant. The Lagrange invariant defines the number of resolvable points that can be steered to [6]. Currently, researchers are looking for beam steering techniques that include such qualities as being compact, lightweight, faster, able to steer over a wide field of view, and consume less power via non-mechanical means.

### 1.2.1 Mechanical Techniques

Mechanical beam steering, as its name suggests, involves movable parts. Such devices that fall under this type of technique include mirrors, micro-electro-mechanical systems (MEMS), micro-opto-electro-mechanical systems (MOEMS), Risley prisms, and decentered lenses. Mirrors, Risley prisms, decentered lenses [4], and microlenses [7] are all macro-optical beam steering devices, which means that they are able to achieve fairly large steering angles. In particular, Risley prisms, which are often comprised of two achromatic prisms in succession along the optical axis, have been shown to steer a beam to a maximum of about  $45^\circ$  by rotating the prisms into various configurations. Decentered lenses, which are achieved by laterally shifting the exit and input lenses with respect to each other, are able to steer a beam at a maximum angle of  $25^\circ$ . On the other end of mechanical beam steering technologies are the micro-optical devices which include MEMS and MOEMS. Such devices as mentioned previously are especially attractive since they are compact, lightweight, and consume less power [4].

### 1.2.2 Non-mechanical Techniques

Mechanical beam steering is definitely attractive for applications in which a large steering angle is necessary. Unfortunately, the problem with this type of beam steering is the need for stability in the environment as well as having to apply a mechanical force to move the components. As a result, non-mechanical beam steering has become attractive for applications in which the optical axis of a device needs to be redirected to various locations at a relatively fast speed or in which the platform is quite small and mechanical stabilization during scanning is difficult to achieve. The goal for many researchers is to

develop technology that maintains the above benefits without compromising the aperture size, efficiency, steering capability [8], and imaging quality.

Non-mechanical beam steering can be implemented through the use of acousto-optic (AO) modulators, optical phased arrays (OPAs), waveguides [5], MEMS actuators [8], and liquid crystal spatial light modulators (LC-SLMs) to name a few. Of these techniques, a LC-SLM has become quite popular because it is cost effective, readily available, and allows for control of the two-dimensional spatial distribution of the phase of light, which is essential for beam steering. However, such a device is polarization dependent, which means that it requires a certain polarization state incident upon it, namely linear polarization oriented at a prescribed direction, in order to steer a beam. Figure 1.1 shows a Boulder Nonlinear Systems (BNS) LC-SLM [9].

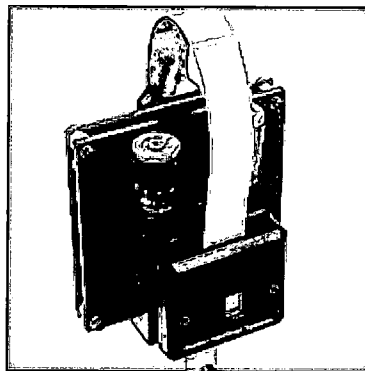


Figure 1.1 Boulder Nonlinear Systems LC-SLM

With a LC-SLM, non-mechanical beam steering is usually accomplished through the use of a stepped phase profile, which is electronically displayed on the device. This stepped phase profile is related to a blazed grating, which is a phase profile in the shape of a sawtooth pattern. It is the slope of the sawtooth that determines the steering angle of an incoming beam which is diffracted into various orders. For the purpose of variable

period beam steering, the first diffraction order is usually the only order of importance while variable blaze beam steering is done by moving from one grating order to the next [6, 10]. Figure 1.2 shows a schematic of a blazed grating [11].

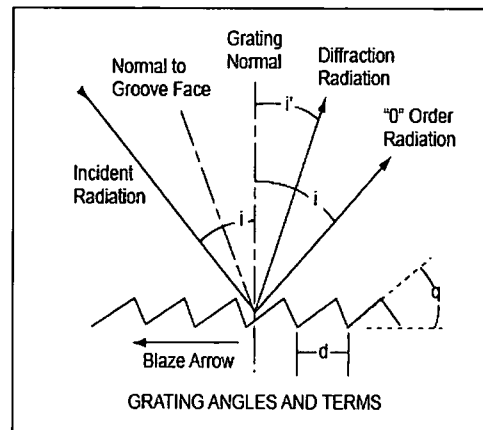


Figure 1.2 Schematic of a blazed grating

Ideally, a blazed grating is comprised of a perfect sawtooth pattern. Unfortunately, this is not the case in realistic systems because of the introduction of a flyback region as well as the phase profile having steps. Flyback relates to a non-perfect blazed edge, which affects the reset of the sawtooth. Figure 1.3 depicts how flyback affects the sawtooth pattern of a blazed grating [5]. The notion of flyback will be discussed in further details in Chapter 2.

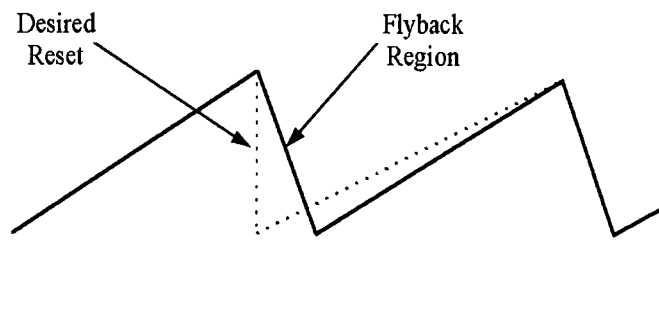


Figure 1.3 Schematic showing the flyback region



## CHAPTER II: BEAM STEERING WITH LC-SLM

### 2.1 Principle

As previously mentioned, a liquid crystal spatial light modulator has become a popular device for non-mechanical beam steering. Figure 2.1 shows a cross-sectional illustration of this device [2, 12].

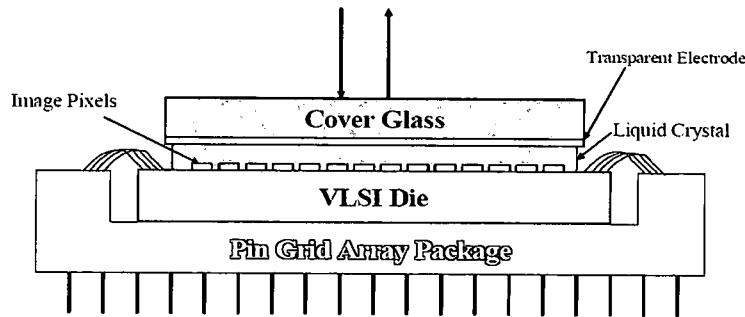


Figure 2.1 Cross-sectional illustration of LC-SLM

From this illustration, light enters the cover glass of the LC-SLM and passes through both the transparent electrode and liquid crystal layers. The beam is then reflected off of the image pixels and returns the way that it came. Electric signals flow through the pin grid array package into the very large scale integration (VLSI) die circuitry, thus applying voltage to each electrode/pixel in order to generate an electric field between each transparent electrode, which is the ground plane, and each patterned electrode. As a result of this field, the birefringence of the liquid crystal layer is changed. For a given linear polarization state incident upon the device, such a change of birefringence leads to phase modulation. Since each pixel is controlled independently, different phase patterns can be displayed onto the LC-SLM by changing the voltages of each pixel [2]. For beam steering applications, such phase patterns are typically in the form of a blazed grating.

Beam steering accomplished through the use of LC-SLMs can be categorized based on the physical methods used to redirect light – refraction and diffraction. Refractive beam steering can be accomplished by a number of means including liquid crystal wedges and devices that use double refraction. Such devices resemble glass prisms in how they operate. A glass prism is able to refract light because its index of refraction differs from air. Overall, refractive beam steering devices offer high efficiency at the cost of the steering angle. The steering angle for a wedge is determined by dividing the angle of the wedge by the aperture, which results in a steering angle on the order of tens of milliradians [13]. The reason for this limit is that the speed of the device is determined by its thickness squared. In other words, the thicker the wedge; the slower its response time will be. Devices using double refraction, where the steering angle is determined by the difference between the ordinary and extraordinary refractive indices, are limited to a few degrees for steering [13].

The other category of beam steering with LC-SLMs deals with diffraction. Diffractive beam steering can be accomplished through the use of an optical phased array (OPA) similar to some radar systems. This diffractive OPA is thought to be like a quantized multiple level phase grating, which means that higher diffraction efficiency can be achieved by increasing the number of phase levels in the array [13]. The ideal diffraction efficiency,  $\eta_{11}$ , can be defined as the ratio of the light intensity of the desired diffraction order,  $I_n$ , and the incident light,  $I_{inc}$ , as shown in the equation below [14, 15]:

$$\eta_{11} = \frac{I_1}{I_{inc}} = \text{sinc}^2\left(\frac{1}{2^M}\right) \quad (1)$$

For beam steering, only the desired diffraction order is considered when calculating the efficiency, which in this case is the first order. Note that  $M$  and  $2^M$  represent the number of quantization steps and phase levels [3], respectively. Table 2.1 gives the calculated diffraction efficiency for  $M$  from one to nine.

Table 2.1 Ideal 1st order diffraction efficiency as a function of the # of phase levels

# of Quantization Steps	Phase Levels	Ideal 1 <sup>st</sup> Order Diffraction Efficiency (%)
1	2	40.53
2	4	81.06
3	8	94.96
4	16	98.72
5	32	99.68
6	64	99.92
7	128	99.98
8	256	99.99
9	512	100

In reality, the phase profile resembles a blazed grating instead of being a series of quantized steps because of fringing field effects between electrodes. This blazed grating is comprised of a sawtooth pattern acting like a continuously increasing phase ramp [16] that goes from zero to  $2\pi$  and then resets as depicted in Figure 2.2 [17].

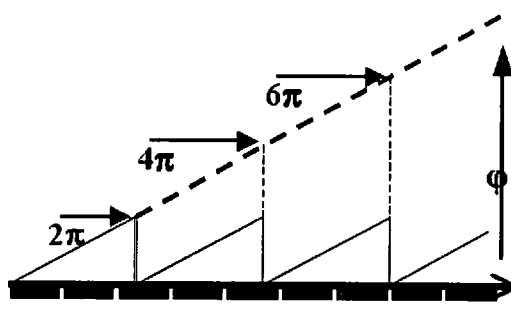


Figure 2.2 Illustration of  $2\pi$  phase reset of blazed grating

The efficiency of the device is not only affected by this phase profile, but it is also affected by the effective fill factor, which takes into account the flyback region. Now this flyback region as mentioned in the previous chapter occurs at the location where the phase reset for a grating period takes place [13]; the resets are defined by the steering angle. Also, this region is sloped with an opposite blaze and remains constant for a given device geometry as the slope of the sawtooth pattern is changed; therefore, the steeper the slope of the sawtooth pattern; the more the diffraction efficiency is affected by flyback. In other words, when steering a beam at the device's maximum angle, the efficiency is highly contingent on the effects of flyback [8]. As a result, the diffraction efficiency for the first order with flyback present can be approximated as [15]

$$\eta_{12} = \left(1 - \frac{\Lambda_F}{\Lambda_g}\right)^2, \quad (2)$$

where  $\Lambda_F$  and  $\Lambda_g$  represent the width of the flyback region and the desired grating period, respectively. Taking the product of equations (1) and (2) yields the overall steering efficiency,  $\eta_d$ , only if the phase profile really is a "stair-step" [15].

$$\eta_d = \eta_{11}\eta_{12} = \left(\text{sinc}^2\left(\frac{1}{2^M}\right)\right) \left(1 - \frac{\Lambda_F}{\Lambda_g}\right)^2 \quad (3)$$

## 2.2 Modeling of Beam Steering with LC-SLM

Having delved into the principle behind using a LC-SLM for beam steering, the focus in this section is to model this application both analytically and numerically. First, the possible steering/diffraction angles,  $\theta$ , (first order only) for a design wavelength,  $\lambda$ , of  $1.064\mu\text{m}$  were computed for various grating periods,  $\Lambda_g$ , by using

$$\theta = \sin^{-1}\left(\frac{\lambda}{\Lambda_g}\right) = \sin^{-1}\left(\frac{\lambda}{N\Lambda_p}\right), \quad (4)$$

where  $\Lambda_p$  and  $N$  are the pixel pitch/size of the LC-SLM and number of pixels for one period, respectively. From equation (4), the steering angle is seen to be inversely proportional to the grating period in the small angle limit. Also, this equation assumes that the first diffraction order is the only order being considered and since  $N$  is an integer number, the steering angle has to be discrete, not a continuous sweep. The LC-SLM that was used for the overall design is a 512 by 512 Boulder Nonlinear Systems (BNS) device with a pixel pitch of  $15\mu\text{m}$  and a linear fill factor of 83.4%. Figure 2.3 presents an illustration of this BNS device [18].

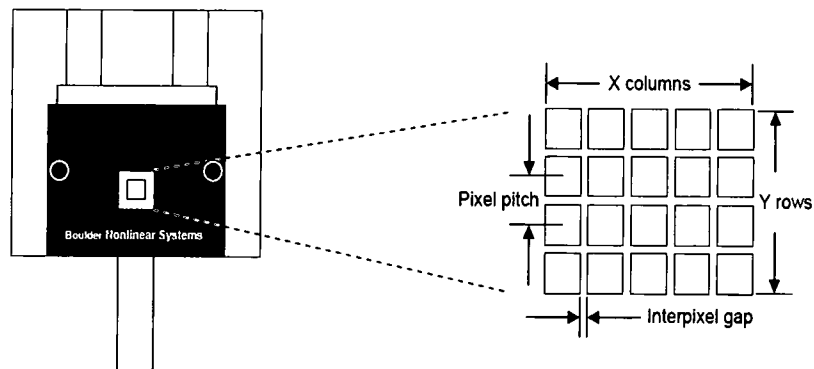


Figure 2.3 Illustration of BNS LC-SLM

Using these values, the theoretical steering angles for the particular BNS device can be calculated. Table 2.2 presents these calculated angles, which depend on the number of pixels per grating period.

**Table 2.2 Theoretical steering angle based on number of pixels per grating period**

<b># of Pixels per Period</b>	<b>Grating Period (mm)</b>	<b>Steering Angle (°)</b>
512	7.68	0.00794
256	3.84	0.01588
128	1.92	0.03175
64	0.96	0.06350
32	0.48	0.12701
16	0.24	0.25401
8	0.12	0.50803
4	0.06	1.0161
2	0.03	2.0325

For the purpose of this calculation, the number of pixels for one grating period was chosen based on powers of two starting with a grating period of two pixels and ending with a grating period of 512 pixels, which is the maximum number of pixels of the liquid crystal in one dimension. As a result, a binary (two pixel) phase grating gives a maximum steering angle of about  $\pm 2^\circ$  for this particular LC-SLM at a wavelength of  $1.064\mu\text{m}$ . Both the possible steering angles and the liquid crystal parameters will be utilized in the numerical model of the device, but first an analytical model must be presented in order to simulate the beam steering operation of the LC-SLM in MatLab.

Note that since this LC-SLM is a two-dimensional array device, it has the additional benefit of being able to steer a beam in two dimensions.

### 2.2.1 Analytical Model

In general, the overall grid of the SLM can be expressed as

$$\{p(x, y) \otimes \text{grid}(n\Delta x, m\Delta y)\} \times \{\text{mask} \times e^{j\phi(x, y)}\}, \quad (5)$$

where  $p(x, y)$ ,  $\text{grid}(n\Delta x, m\Delta y)$ ,  $\text{mask}$  and  $e^{j\phi(x, y)}$  represent the pixel pattern, grid function, mask of the SLM, and phase of the SLM, respectively. Note that  $\otimes$  represents a convolution. The pixel pattern and mask of the SLM can be represented by a rectangle function while the grid function is given as a comb function. This expression is relevant for a fill factor of 100%, which of course is the ideal case. Realistically, the particular device to be used has a fill factor of 83.4% according to the manufacturer's specifications, which needs to be taken into consideration. Therefore, after reflecting off of the LC-SLM, a normally incident plane wave in only the  $x$  dimension for simplicity can be modeled as

$$\begin{aligned} f(x) = & \left( \text{comb}\left(\frac{x}{\Lambda_p}\right) \otimes \text{rect}\left(\frac{x}{\eta_{ff}\Lambda_p}\right) \right) \left( \left( e^{ikx \sin \theta} \text{rect}\left(\frac{x}{M\Lambda_p}\right) \right) \otimes \text{comb}\left(\frac{x}{M\Lambda_p}\right) \right) \text{rect}\left(\frac{x}{N\Lambda_p}\right) \\ & + \left( \text{comb}\left(\frac{x}{\Lambda_p}\right) \otimes \left[ \text{rect}\left(\frac{x}{\Lambda_p}\right) - \text{rect}\left(\frac{x}{\eta_{ff}\Lambda_p}\right) \right] \right) \text{rect}\left(\frac{x}{N\Lambda_p}\right) \end{aligned} \quad (6)$$

where  $\eta_{ff}$ ,  $\Lambda_p$ ,  $M$ ,  $N$ , and  $\theta$  represent the fill factor, pixel pitch, number of pixels in one period, total number of pixels in  $x$  dimension, and steering angle, respectively. The first portion of this expression is comprised of the pixel pattern of the entire mask of the SLM

with a discretized phase pattern present due to a periodic blazed grating while the second portion takes into account the gap between pixels caused by the fill factor being less than 100%. By analytical means, the Fourier transform of this expression becomes

$$F(k_x) = \left( \frac{1}{|K_x|} \text{comb} \left( \frac{k_x}{K_x} \right) \frac{\eta_f}{|K_x|} \text{sinc} \left( \frac{\eta_f k_x}{K_x} \right) \right) \otimes \left( \frac{M}{|K_x|} \text{sinc} \left( \frac{M(k_x - k \sin \theta)}{K_x} \right) \frac{M}{|K_x|} \text{comb} \left( \frac{M k_x}{K_x} \right) \right) \otimes \frac{N}{|K_x|} \text{sinc} \left( \frac{N k_x}{K_x} \right) + \left( \left\{ \frac{1}{|K_x|} \text{comb} \left( \frac{k_x}{K_x} \right) \left[ \frac{1}{|K_x|} \text{sinc} \left( \frac{k_x}{K_x} \right) - \frac{\eta_f}{|K_x|} \text{sinc} \left( \frac{\eta_f k_x}{K_x} \right) \right] \right\} \otimes \frac{N}{|K_x|} \text{sinc} \left( \frac{N k_x}{K_x} \right) \right), \quad (7a)$$

where  $K_x$  is defined as  $2\pi/\Lambda_p$  in this model. This expression can be rewritten as

$$F(k_x) = \left( \frac{\eta_f}{|K_x|^2} \text{comb} \left( \frac{k_x}{K_x} \right) \text{sinc} \left( \frac{\eta_f k_x}{K_x} \right) \right) \otimes \left( \frac{M^2}{|K_x|^2} \text{sinc} \left( \frac{M(k_x - k \sin \theta)}{K_x} \right) \text{comb} \left( \frac{M k_x}{K_x} \right) \right) \otimes \frac{N}{|K_x|} \text{sinc} \left( \frac{N k_x}{K_x} \right) + \left( \left\{ \frac{1}{|K_x|^2} \text{comb} \left( \frac{k_x}{K_x} \right) \left[ \text{sinc} \left( \frac{k_x}{K_x} \right) - \eta_f \text{sinc} \left( \frac{\eta_f k_x}{K_x} \right) \right] \right\} \otimes \frac{N}{|K_x|} \text{sinc} \left( \frac{N k_x}{K_x} \right) \right). \quad (7b)$$

From expression (7b), the first and second sinc and comb function combinations relate to the individual pixels and the sawtooth pattern, respectively. Furthermore, the second sinc and comb combination results in a discrete phase pattern rather than a continuous sweep of the angle. The sinc function at the end of lines two and three of the expression relates to the overall mask of the SLM. Finally, the third sinc and comb function combination represents the fixed pattern of the SLM when the fill factor is not 100%. With a 100% fill factor, this second line disappears. Taking the expression from (7b), the beam



steering capability of the LC-SLM can be modeled using the MatLab computational software as shown in Figures 2.4 and 2.5.

Both figures show the diffraction efficiency versus the diffraction angle. In the MatLab code, conv1 and conv2 represent the first and second portions of the beam steering expression presented in expression (7b), respectively. In other words, conv1 is representative of the far field diffraction due to the LC-SLM pixel pattern while conv2 corresponds to the far field diffraction due to the gaps in the pixel pattern. Figure 2.4 shows a plot of the maximum steering angle of  $2.0325^\circ$  while Figure 2.5 shows three different angles –  $0.50803^\circ$ ,  $1.0161^\circ$ , and  $2.0325^\circ$  – overlaid on the same plot in order to simulate the discrete steering of the beam.

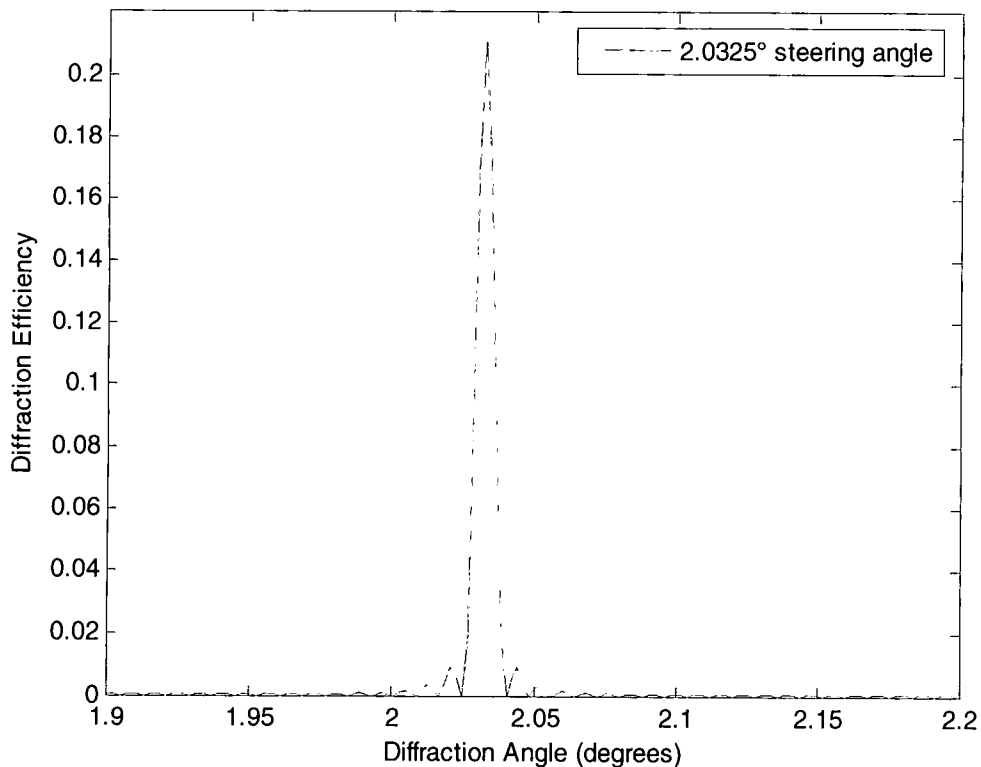


Figure 2.4 Analytical model for a steering angle of about  $2^\circ$

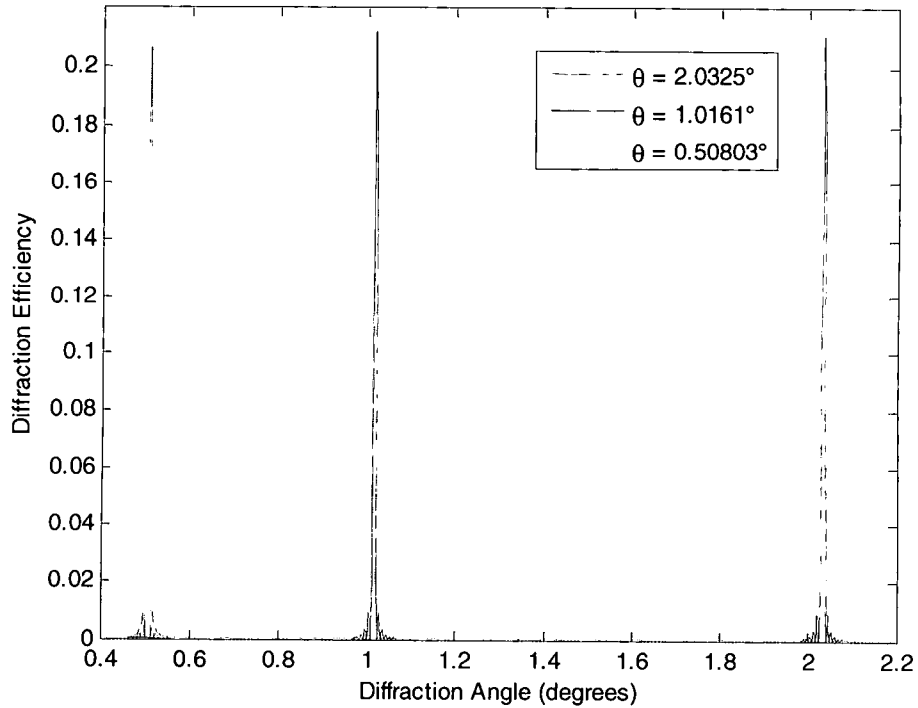


Figure 2.5 Analytical model for steering angles of about 0.5°, 1°, and 2°

From both of these plots, the diffraction efficiency for the three different steering angles shown is 21.09%. The efficiency is the same for the three steering angles because the discrete phase level is not considered in the analytical model; therefore, the MatLab code only deals with a pure phase blazed grating. See Appendix A.1 for the MatLab code.

### 2.2.2 Numerical Model

A numerical model of the beam steering capability with a discretized phase pattern can be obtained using MatLab as well. For this model, an array is defined for the SLM mask in the  $x$  dimension only for simplicity, mapped into  $k$  space, and then zero padded. The desired phase is obtained from the corresponding transmittance function in the  $x$  dimension and then discretized in order to be displayed on the SLM. Next, the

transmittance function of the SLM is defined using the discrete phase pattern, Fourier transformed, and then it is normalized. Finally, the  $k$  space is mapped into the corresponding angle and the fill factor squared is multiplied by the normalized intensity in order to obtain the appropriate diffraction efficiency values for the different steering angles. Both figures show the diffraction efficiency plotted versus the diffraction angle. Figure 2.6 shows a plot of the maximum steering angle of  $2.0325^\circ$  with a diffraction efficiency of about 39.5% and 27.5% for the case of a 100% and 83.4% fill factor, respectively. Note that since the maximum steering angle case is for a binary phase grating, there are symmetric peaks at about  $\pm 2^\circ$ .

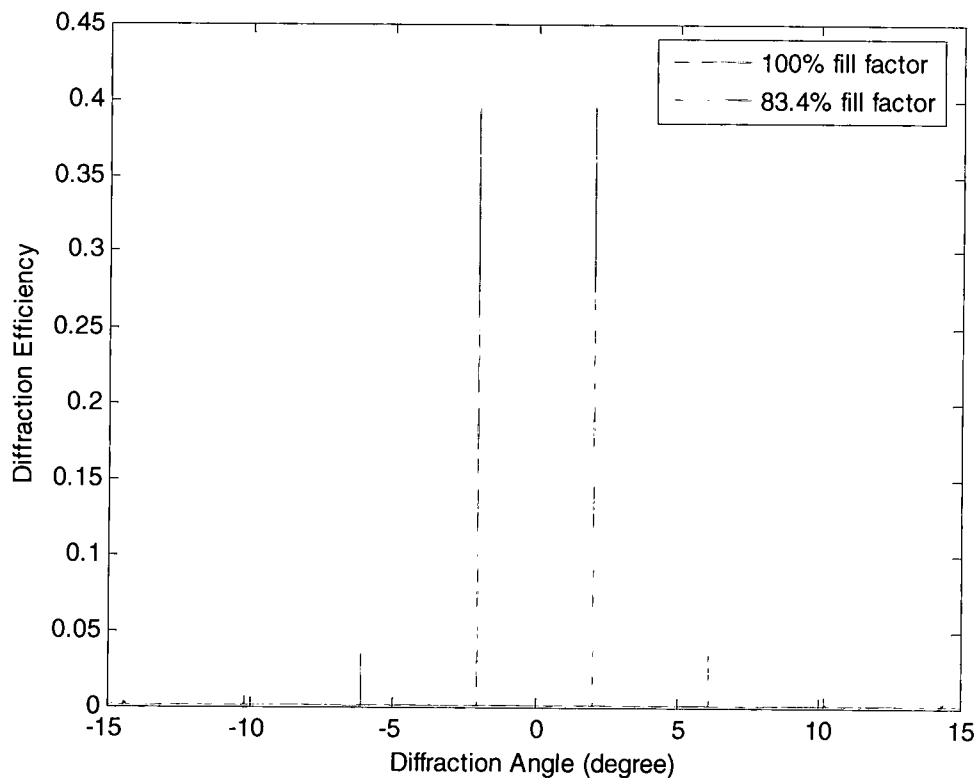


Figure 2.6 Numerical model for a steering angle of about  $2^\circ$

Figure 2.7 shows three angles –  $0.50803^\circ$ ,  $1.0161^\circ$ , and  $2.0325^\circ$  – overlaid on the same plot as was done in Figure 2.5, thus simulating the beam being steered. The difference between Figures 2.7 and 2.5 is that the diffraction efficiency for each angle is different. For steering angles of  $0.50803^\circ$ ,  $1.0161^\circ$ , and  $2.0325^\circ$  with a 100% fill factor, the diffraction efficiency is 94.8%, 80.5%, and 39.5%, respectively. These efficiencies correlate to those presented in Table 2.1. For the actual fill factor of 83.4%, the efficiencies for the three angles from about  $0.5^\circ$  to  $2^\circ$  are 66%, 56%, and 27.5%, respectively. See Appendix A.2 for the MatLab code.

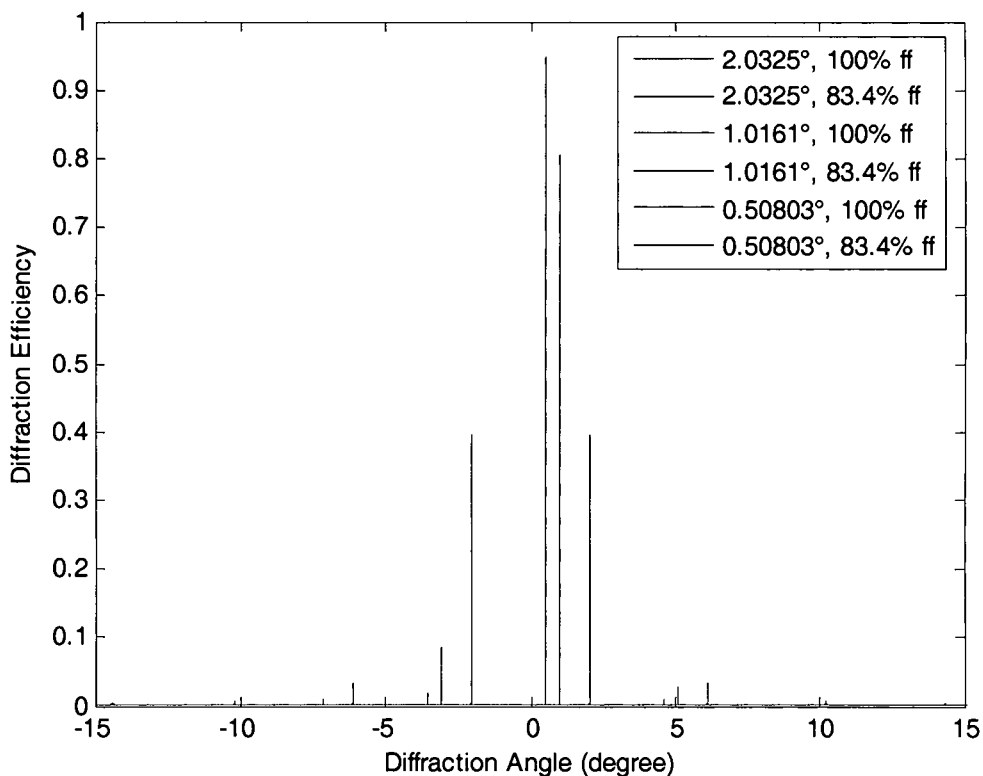


Figure 2.7 Numerical model for steering angles of about  $0.5^\circ$ ,  $1^\circ$ , and  $2^\circ$

### 2.3 Polarization Issues

Since the LC-SLM is polarization dependent, it requires a linear polarization state incident upon it in order for beam steering to occur. As mentioned earlier, the separation of transmitter and receiver was previously addressed through the use of a circularly polarized beam and a polarization beam splitter. Unfortunately, this method results in a power loss of at least 50% since only one of the linear components of the circularly polarized beam is used. In order to overcome this drawback, a new Tx/Rx switch is designed with the use of a large aperture Faraday rotator. The proposed efficient Tx/Rx switch design is discussed in further detail in the next chapter. Also, a polarization study is presented using Jones calculus.

## CHAPTER III: EFFICIENT TRANSMIT/RECEIVE SWITCH

### 3.1 Design and Principle

A current issue with a LC-SLM for non-mechanical beam steering is producing a more efficient transmit/receive (Tx/Rx) switch for such applications as laser scanning imaging and remote sensing systems. As previously mentioned, a traditional Tx/Rx switch has been done using a circularly polarized beam obtained from a quarter-wave plate in conjunction with a polarization beam splitter, which leads to a very lossy solution. In order to overcome some of the drawbacks of this previous design, beam steering based on a two-dimensional (2-D) reflection type LC-SLM being used in conjunction with a large, clear aperture (20mm) Faraday rotator, which was not previously available, is proposed and tested. Higher diffraction efficiency, good imaging quality, and developing a more compact layout sometime in the future are expected. Because of the substantial size of the magnet housing of the Faraday rotator, making the design more compact will be difficult.

This large, clear aperture Faraday rotator from Electro-Optics Technology (EOT) acts as an isolator between the transmitter and receiver of the design and rotates the polarization of light. Based on the manufacturer's specifications of this particular device, the rotation, transmission, and extinction were tested to be  $44.5^\circ$ , 99%, and 40dB, respectively. For simplicity, a  $45^\circ$  rotation angle for the Faraday rotator will be used in the section about the polarization study via Jones calculus.

### 3.1.1 Design Schematic

The beam steering aspect of the LC-SLM has been modeled both analytically and numerically based on the given specifications. Also, the proposed Tx/Rx switch design has been briefly discussed in respect to the addition of a large, clear aperture Faraday rotator. At this point, it is essential to delve further into the overall design of an efficient Tx/Rx switch design for beam steering with a LC-SLM. Figure 3.1 shows a schematic of the proposed design.

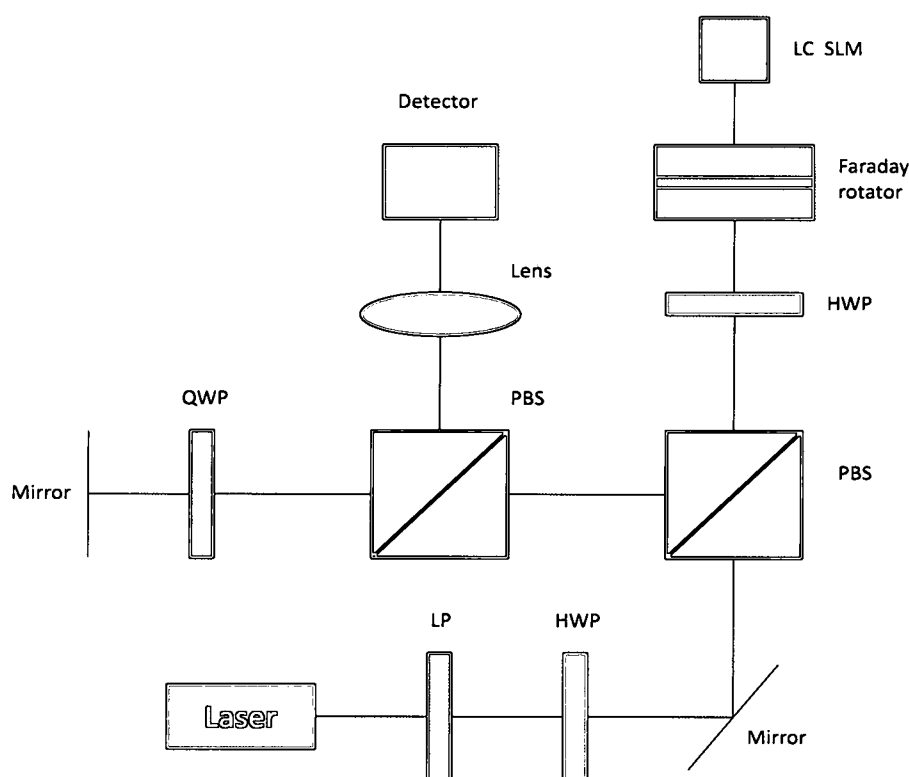


Figure 3.1 Schematic of the Tx/Rx switch design

From this figure, a linearly polarized beam is emitted from a laser source and passes through both a linear polarizer (LP), which acts as a variable attenuator, and a half-wave plate (HWP), which matches the beam's polarization to the s- or p-polarization state of the first polarization beam splitter (PBS). Following this PBS, a second half-wave plate

in conjunction with the Faraday rotator is used to obtain the desired linearly polarized beam incident upon the LC-SLM. Next, the beam propagates through the large, clear aperture Faraday rotator, which rotates the polarization of the incoming beam by  $45^\circ$ . The Faraday rotator also acts as an isolator for the Tx/Rx switch since it is used to protect the laser source from any damaging back reflection [19]. After the Faraday rotator, the linearly polarized beam is reflected off the LC-SLM at a desired steering angle based on the blazed grating displayed on the device. This beam is then sent back through both the Faraday rotator and the HWP allowing for maximum power throughput to be sent to the second PBS.

The second portion shown in this figure is the receiver end of the switch where the beam is transmitted through a second polarization beam splitter to a quarter-wave plate (QWP). When the beam passes through this QWP, it is changed from a linearly polarized beam to either a right- or left-handed circularly polarized (RCP or LCP) beam. This circularly polarized beam changes handedness upon reflection off of a mirror, which is simulating a target. In other words, if the incoming beam is RCP, it becomes LCP after reflection and vice versa. This reflected beam then passes through the QWP again resulting in the opposite linear polarization state that was originally transmitted through the second PBS. As a result, the beam is directed towards a lens which images the beam onto a detector. This design was confirmed by a simple polarization study using Jones calculus [20, 21].



### 3.1.2 Polarization Study via Jones Calculus

Starting with a collimated laser beam, the beam passes through a linear polarizer that either polarizes the beam horizontally or vertically. For the purpose of this study, the linear polarizer is vertically polarized, which results in a vertically polarized beam.

$$\begin{bmatrix} 0 & 0 \\ 0 & 1 \end{bmatrix} \begin{bmatrix} 1 \\ 1 \end{bmatrix} = \begin{bmatrix} 0 \\ 1 \end{bmatrix} \quad (8)$$

The vertically polarized beam then propagates through a half-wave ( $\lambda/2$ ) plate yielding the following polarization.

$$\begin{bmatrix} j & 0 \\ 0 & -j \end{bmatrix} \begin{bmatrix} 0 \\ 1 \end{bmatrix} = \begin{bmatrix} 0 \\ -j \end{bmatrix} \quad (9)$$

Next, the beam goes through a vertically polarized beam splitter, which transmits the entire beam.

$$\begin{bmatrix} 0 & 0 \\ 0 & 1 \end{bmatrix} \begin{bmatrix} 0 \\ -j \end{bmatrix} = \begin{bmatrix} 0 \\ -j \end{bmatrix} \quad (10)$$

After the PBS, the linearly polarized beam is rotated at  $\theta = \frac{\pi}{8} + \frac{\pi}{2} = \frac{5\pi}{8}$  by a second HWP.

$$\begin{aligned} & \begin{bmatrix} \cos(-\theta) & \sin(-\theta) \\ -\sin(-\theta) & \cos(-\theta) \end{bmatrix} \begin{bmatrix} j & 0 \\ 0 & -j \end{bmatrix} \begin{bmatrix} \cos(\theta) & \sin(\theta) \\ -\sin(\theta) & \cos(\theta) \end{bmatrix} \begin{bmatrix} 0 \\ -j \end{bmatrix} \\ &= \frac{\sqrt{2}}{2} \begin{bmatrix} -j & -j \\ -j & j \end{bmatrix} \begin{bmatrix} 0 \\ -j \end{bmatrix} = \frac{\sqrt{2}}{2} \begin{bmatrix} -1 \\ 1 \end{bmatrix} \end{aligned} \quad (11)$$

The beam then propagates through the Faraday rotator, which rotates the beam by  $45^\circ$ .

$$\begin{bmatrix} \cos\left(\frac{\pi}{4}\right) & -\sin\left(\frac{\pi}{4}\right) \\ \sin\left(\frac{\pi}{4}\right) & \cos\left(\frac{\pi}{4}\right) \end{bmatrix} \frac{\sqrt{2}}{2} \begin{bmatrix} -1 \\ 1 \end{bmatrix} = \left(\frac{\sqrt{2}}{2}\right) \left(\frac{\sqrt{2}}{2}\right) \begin{bmatrix} 1 & -1 \\ 1 & 1 \end{bmatrix} \begin{bmatrix} -1 \\ 1 \end{bmatrix} = \frac{1}{2} \begin{bmatrix} -2 \\ 0 \end{bmatrix} = \begin{bmatrix} -1 \\ 0 \end{bmatrix} \quad (12)$$

The resulting linearly polarized beam is then reflected off of the LC-SLM. Note that the LC-SLM is being represented as a perfect mirror, thus neglecting any phase.

$$\begin{bmatrix} 1 & 0 \\ 0 & -1 \end{bmatrix} \begin{bmatrix} -1 \\ 0 \end{bmatrix} = \begin{bmatrix} -1 \\ 0 \end{bmatrix} \quad (13)$$

After reflection off of the LC-SLM, the beam returns through both the Faraday rotator (14), which now rotates the beam by  $-45^\circ$ , and the HWP (15), which is now rotated at

$$\theta = \frac{\pi}{2} - \frac{\pi}{8} = \frac{3\pi}{8}.$$

$$\begin{bmatrix} \cos\left(-\frac{\pi}{4}\right) & -\sin\left(-\frac{\pi}{4}\right) \\ \sin\left(-\frac{\pi}{4}\right) & \cos\left(-\frac{\pi}{4}\right) \end{bmatrix} \begin{bmatrix} -1 \\ 0 \end{bmatrix} = \frac{\sqrt{2}}{2} \begin{bmatrix} 1 & 1 \\ -1 & 1 \end{bmatrix} \begin{bmatrix} -1 \\ 0 \end{bmatrix} = \frac{\sqrt{2}}{2} \begin{bmatrix} -1 \\ 1 \end{bmatrix} \quad (14)$$

$$\begin{bmatrix} \cos(-\theta) & \sin(-\theta) \\ -\sin(-\theta) & \cos(-\theta) \end{bmatrix} \begin{bmatrix} j & 0 \\ 0 & -j \end{bmatrix} \begin{bmatrix} \cos(\theta) & \sin(\theta) \\ -\sin(\theta) & \cos(\theta) \end{bmatrix} \frac{\sqrt{2}}{2} \begin{bmatrix} -1 \\ 1 \end{bmatrix} \quad (15)$$

$$= \left(\frac{\sqrt{2}}{2}\right) \left(\frac{\sqrt{2}}{2}\right) \begin{bmatrix} -j & j \\ j & j \end{bmatrix} \begin{bmatrix} -1 \\ 1 \end{bmatrix} = \frac{1}{2} \begin{bmatrix} 2j \\ 0 \end{bmatrix} = \begin{bmatrix} j \\ 0 \end{bmatrix}$$

Ideally, 100% of the beam is transmitted to the receiver portion of the setup by the second polarization beam splitter, which means that there is no transmission back to the laser.

$$\begin{bmatrix} 1 & 0 \\ 0 & 0 \end{bmatrix} \begin{bmatrix} j \\ 0 \end{bmatrix} = \begin{bmatrix} j \\ 0 \end{bmatrix} \quad (16)$$

At this point, the beam passes through the second PBS with no change in polarization.

$$\begin{bmatrix} 1 & 0 \\ 0 & 0 \end{bmatrix} \begin{bmatrix} j \\ 0 \end{bmatrix} = \begin{bmatrix} j \\ 0 \end{bmatrix} \quad (17)$$

This linearly polarized beam passes through a quarter-wave ( $\lambda/4$ ) plate rotated at  $\theta = \frac{\pi}{4}$ .

$$\begin{aligned}
& \begin{bmatrix} \cos(-\theta) & \sin(-\theta) \\ -\sin(-\theta) & \cos(-\theta) \end{bmatrix} \begin{bmatrix} 1 & 0 \\ 0 & j \end{bmatrix} \begin{bmatrix} \cos(\theta) & \sin(\theta) \\ -\sin(\theta) & \cos(\theta) \end{bmatrix} \begin{bmatrix} j \\ 0 \end{bmatrix} \\
&= \begin{bmatrix} \cos^2(\theta) + j \sin^2(\theta) & \cos(\theta)\sin(\theta) - j \cos(\theta)\sin(\theta) \\ \cos(\theta)\sin(\theta) - j \cos(\theta)\sin(\theta) & \sin^2(\theta) + j \cos^2(\theta) \end{bmatrix} \begin{bmatrix} j \\ 0 \end{bmatrix} \\
&= \begin{bmatrix} -\sin^2(\theta) + j \cos^2(\theta) \\ \cos(\theta)\sin(\theta) + j \cos(\theta)\sin(\theta) \end{bmatrix} = \begin{bmatrix} -\frac{1}{2} + j\frac{1}{2} \\ \frac{1}{2} + j\frac{1}{2} \end{bmatrix} = \frac{1}{2} \begin{bmatrix} -1 + j \\ 1 + j \end{bmatrix} \\
&= \frac{1}{2}(-1 + j) \begin{bmatrix} 1 \\ -j \end{bmatrix}
\end{aligned} \tag{18}$$

A left-handed circularly polarized beam is then reflected off of a mirror, which is simulating a target, to become a right-handed circularly polarized beam.

$$\begin{bmatrix} 1 & 0 \\ 0 & -1 \end{bmatrix} \frac{1}{2}(-1 + j) \begin{bmatrix} 1 \\ -j \end{bmatrix} = \frac{1}{2}(-1 + j) \begin{bmatrix} 1 \\ j \end{bmatrix} \tag{19}$$

The reflected beam returns through the QWP which is rotated at  $\theta = -\frac{\pi}{4}$ .

$$\begin{aligned}
& \begin{bmatrix} \cos(-\theta) & \sin(-\theta) \\ -\sin(-\theta) & \cos(-\theta) \end{bmatrix} \begin{bmatrix} 1 & 0 \\ 0 & j \end{bmatrix} \begin{bmatrix} \cos(\theta) & \sin(\theta) \\ -\sin(\theta) & \cos(\theta) \end{bmatrix} \frac{1}{2}(-1 + j) \begin{bmatrix} 1 \\ j \end{bmatrix} \\
&= \begin{bmatrix} \cos^2(\theta) + j \sin^2(\theta) & \cos(\theta)\sin(\theta) - j \cos(\theta)\sin(\theta) \\ \cos(\theta)\sin(\theta) - j \cos(\theta)\sin(\theta) & \sin^2(\theta) + j \cos^2(\theta) \end{bmatrix} \frac{1}{2}(-1 + j) \begin{bmatrix} 1 \\ j \end{bmatrix} \\
&= \frac{1}{2}(-1 + j) \begin{bmatrix} \cos^2(\theta) + \cos(\theta)\sin(\theta) + j[\sin^2(\theta) + \cos(\theta)\sin(\theta)] \\ -\cos^2(\theta) + \cos(\theta)\sin(\theta) - j[\sin^2(\theta) + \cos(\theta)\sin(\theta)] \end{bmatrix} \\
&= \frac{1}{2}(-1 + j) \begin{bmatrix} 0 \\ -1 \end{bmatrix} = \frac{1}{2} \begin{bmatrix} 0 \\ 1 - j \end{bmatrix}
\end{aligned} \tag{20}$$

Finally, 100% of the beam is ideally transmitted to where the lens and detector are located while no transmission is sent back to the laser. The final polarization state of the beam is

$$\begin{bmatrix} 0 & 0 \\ 0 & 1 \end{bmatrix} \frac{1}{2} \begin{bmatrix} 0 \\ 1-j \end{bmatrix} = \frac{1}{2} \begin{bmatrix} 0 \\ 1-j \end{bmatrix}, \quad (21)$$

which is the Jones matrix representation of a vertically linearly polarized beam incident on the detector.

For this simple polarization study, a few assumptions were made including no leakage from the polarized beam splitters as well as the LC-SLM acting as an ideal mirror. In reality, some leakage will inevitably occur when propagating the beam through both beam splitters. Also, scattering, absorption, and reflection losses from the chain of optics will occur. For this design, the goal is to minimize the amount of leakage in comparison to previous Tx/Rx switch designs.

### 3.1.3 Polarization Study via Schematic

For a more visual look of the polarization study, Figure 3.2 depicts the change of polarization state of the beam as it propagates through the chain of optics.

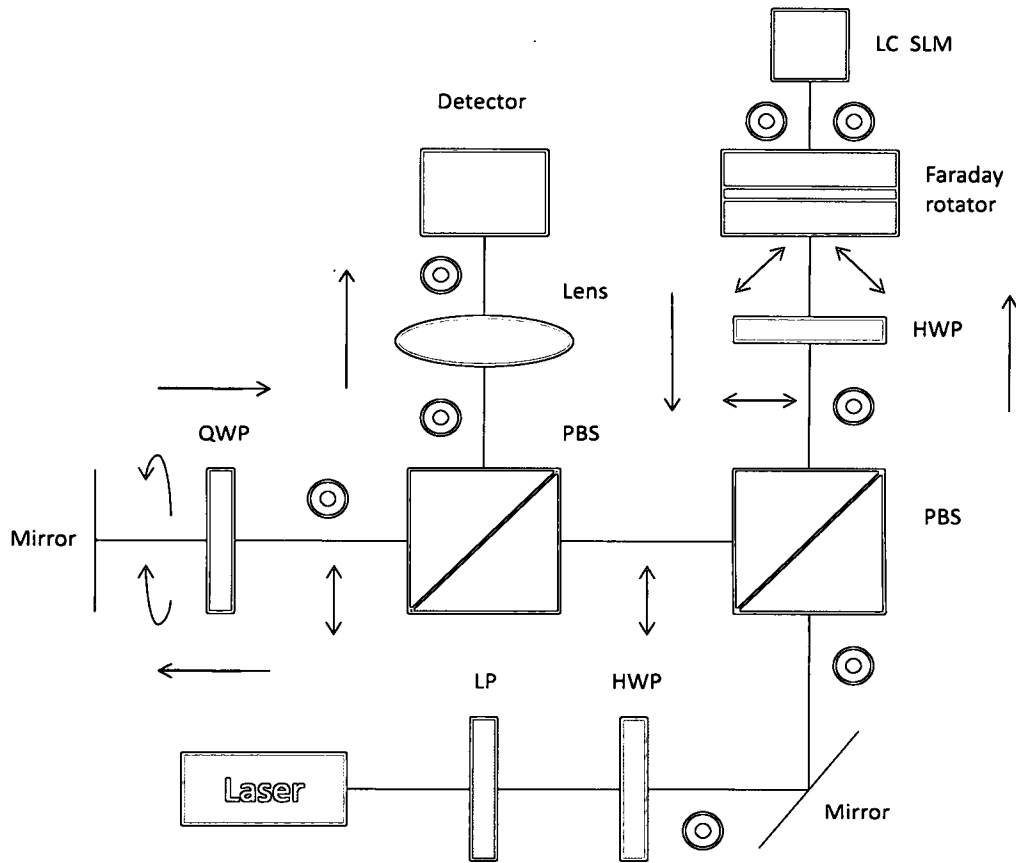


Figure 3.2 Schematic showing polarization states

From this figure, high throughput is expected. Also, since imaging is controlled by the receiver portion of the design, the imaging quality should not be affected because the second polarization beam splitter and quite possibly the lens are the only components that would introduce aberrations in this portion of the setup.

### 3.2 Experimental Verification

Having modeled the beam steering application of the LC-SLM and verified that a linearly polarized beam is indeed incident upon this device, the next step is to present the experimental verification. In this section, the overall setup as well as the results of the power analysis for two different steering angles is shown. Figure 3.3 shows the

experimental setup with LP and PBS representing the linear polarizer and polarization beam splitter, respectively.

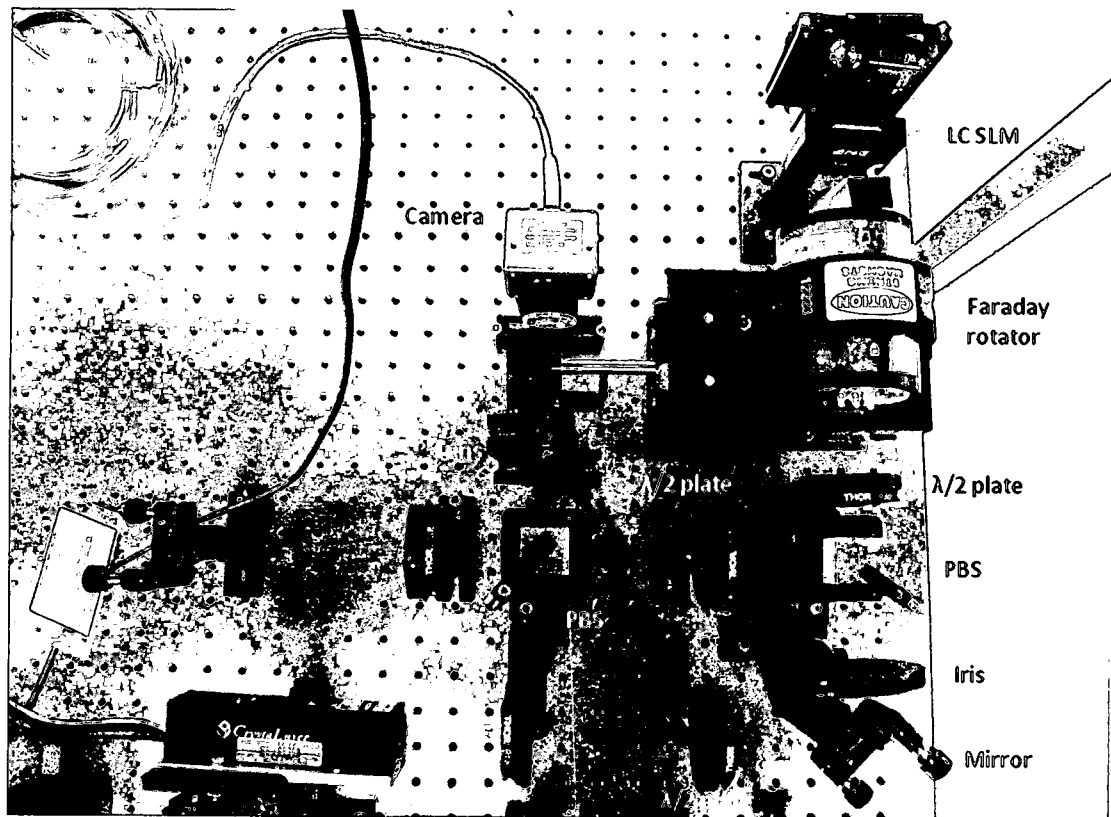


Figure 3.3 Experimental setup

During the alignment process of this design, another half-wave plate, which is not present in the schematic of the design (Figure 3.1), was added between the two polarization beam splitters. This additional half-wave plate is necessary for controlling the polarization of the beam through the second polarization beam splitter, thus maximizing throughput to the detector and/or CCD camera. Also, an iris was placed between the mirror and the first polarization beam splitter in order to block any possible reflections back to the laser or scattering of the beam from the mirror.

From this figure, the laser source that is being used is a diode-pumped infrared Nd:YAG/YVO4 crystal laser (CrystaLaser IRCL-300-1064-S) operating at a wavelength of 1.064 $\mu$ m. All optical components shown are designed for this wavelength including the Faraday rotator (EOT). This particular Faraday rotator has a 20mm clear aperture and is designed to rotate the polarization of an incoming beam by about 45° as previously mentioned. The mirror found after the quarter-wave plate is simulating a target due to the lack of table space in the lab. Finally, there is a 100mm lens imaging the beam onto a CCD camera (Spiricon).

With this setup, a power analysis of the entire system for two different steering angles was conducted in order to obtain the overall diffraction efficiency of the design. First, the transmission capability of the Faraday rotator was tested by measuring the power at locations P3 and P4 in Figure 3.4. The transmission was calculated to be 97.22% ( $P4/P3$ ), which is comparable to the manufacturer's specifications of 99% transmission. The power measurements are presented in Table 3.1. After verifying the transmission of the Faraday rotator, the isolation and extinction of the transmit portion of the setup (right portion as shown in Figure 3.4) were tested. Figure 3.4 shows the schematic of the Tx/Rx switch including the positions where the power measurements were taken.

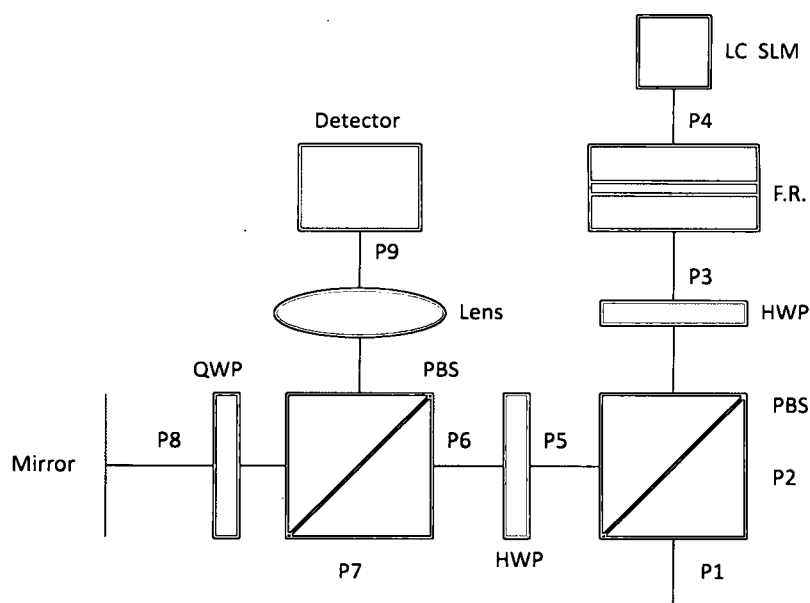


Figure 3.4 Schematic for power measurements of Tx/Rx switch

In order to accomplish this, the LC-SLM was taken out of the setup and replaced by a mirror. The power was then measured at positions P1 through P9 and recorded in Table 3.1.

Table 3.1 Power measurements for mirror in place of LC-SLM

Position	Power (mW)
P1	53.5
P2	1.44
P3	50.4
P4	49.0
P5	47.4
P6	47.1
P7	0.30
P8	46.0
P9	38.1



From this table, the extinction ratio of the transmit portion of the setup was calculated by taking the ratio of the power measured at location P1, which is before the first beam splitter, and the power measured at location P2, which is to the right of it. An extinction ratio of 37.15:1 was obtained. Now it should be noted that the linear polarizer, half-wave plates, and quarter-wave plate used in this design have extinction ratios of 100:1, thus establishing the theoretical limit for the overall design. Next, the isolation capability of the Faraday rotator, HWP, and PBS was tested by measuring the power before the Faraday rotator, P3, and to the left of the first beam splitter, P5. This isolation ratio was calculated to be about 1.0633:1.0, which means that for every 1.0633mW of power that goes into the Faraday rotator, 1mW of power comes out to the left of the first PBS. The overall efficiency was calculated to be 71.2% ( $P_9/P_1$ ). This value is lower than expected because of losses in the chain of optics. Figure 3.4 shows where all of these measurements were taken.

Having successfully tested the isolation capability of the Faraday rotator, the LC-SLM was placed back into the setup without any diffraction pattern displayed on it (zeroth order), thus having it act as a mirror. However, even without a diffraction pattern displayed, the fixed periodic pixel pattern and non-perfect duty cycle of the LC-SLM still cause the incident light to diffract, which ultimately reduces the total amount of power available for beam steering. The available power that is transmitted to the second polarization beam splitter can be calculated from the area of the pixel. For this particular LC-SLM, the linear fill factor is 83.4%, which gives a pixel area of 69.6% and relates to a power loss of 30.4%. Note that the field is attenuated by a linear fill factor while the

irradiance is attenuated by the fill factor squared. According to the data sheet, this BNS LC-SLM has a maximum diffraction efficiency of 61.5% for the zeroth order. In comparison, the diffraction efficiency calculated from the power measured at P4 and P5 from Table 3.2 was 53.67%, which is mainly due to the diffraction effect of the LC-SLM with losses related to the Faraday rotator, HWP, and first PBS.

By not displaying any diffraction pattern on the LC-SLM, the power was measured for the zeroth order of the beam. For beam steering, it is the first order of a beam that is considered. As a result, the final step in determining the overall diffraction efficiency of the design is to actually display a blazed grating [3] for a particular steering angle on the LC-SLM. For the purposes of verifying the design, two different steering angles were considered –  $2.0325^\circ$  and  $1.0161^\circ$ .

First, the phase profile used to steer the beam at a maximum angle of  $2.0325^\circ$  was displayed on the SLM. All power measurements from P1 to P4 do not change since the beam has yet to be diffracted at those locations. After the beam is reflected off of the LC-SLM, it is diffracted into several orders. Most of these orders are blocked by the Faraday rotator on the return pass due to the size of the aperture. However, the first order as previously mentioned is really the only one considered for beam steering with this device. As a result, an iris was placed between the first polarization beam splitter and the additional half-wave plate in order to block the zeroth order of the beam, thus allowing only the power of the first order to be measured throughout the receiver portion of the

design. Power measurements at locations P5 to P9 as shown in Figure 3.4 were recorded in Table 3.2 along with the measurements obtained for the zeroth order.

Table 3.2 Power measurements for 2.0325° steering angle

Position	Power (mW)	
	Zeroth Order	First Order
P1	53.5	53.5
P2	1.44	1.44
P3	50.4	50.4
P4	49.0	49.0
P5	26.3	14.5
P6	26.1	14.3
P7	0.10	0.53
P8	23.8	10.0
P9	19.9	9.3

From this table, the efficiency drops about 50% between the zeroth and first orders of the beam as measured at locations P5 to P9. The overall diffraction efficiency of the first order of the 2.0325° steering angle is 19.06% (P9/P4), 18.45% (P9/P3), or 17.94% (P9/P1) depending on whether the efficiency is calculated from before or after the Faraday rotator or before the first polarization beam splitter. The ideal theoretical diffraction efficiency at the maximum steering angle for the first order was shown to be 40.5% in Chapter 2, which does not take into account any losses in the chain of optics. When this number is multiplied by the LC-SLM's maximum diffraction efficiency of 61.5% for the zeroth order, the theoretical limit for the first order at the maximum

steering angle becomes 24.9%. The 19.06% experimental efficiency is comparable to this theoretical limit.

Using the same procedure from the  $2.0325^\circ$  steering angle case, a phase profile was displayed on the LC-SLM for a  $1.0161^\circ$  steering angle. This angle pertains to a phase profile with a period of four pixels as opposed to the  $2.0325^\circ$  steering angle case which was for a binary phase profile (two pixels per period). Again, the power measurements from P1 to P4 remain the same for both orders – zeroth and first – as well as the measurements from P5 to P9 for the zeroth order. As a result, only the power measurements from P5 to P9 for the first order are different from the previous table. In order to just measure the first order, an iris was again utilized to block the zeroth order of the beam. In comparison to the  $2.0325^\circ$  steering angle case, blocking the zeroth order for this  $1.0161^\circ$  steering angle case was much more difficult because of the closer proximity of the two orders. Table 3.3 presents the power measurements obtained for this steering angle.

**Table 3.3 Power measurements for 1.0161° steering angle**

Position	Power (mW)	
	Zeroth Order	First Order
P1	53.5	53.5
P2	1.44	1.44
P3	50.4	50.4
P4	49.0	49.0
P5	26.3	18.0
P6	26.1	17.5
P7	0.10	0.44
P8	23.8	15.3
P9	19.9	12.6

From this table, there is slightly less of a drop-off in efficiency between the zeroth and first orders. This drop-off in efficiency is about 35%. Overall, the diffraction efficiency of the design was calculated to be 25.71% ( $P_9/P_4$ ), 25% ( $P_9/P_3$ ), or 23.55% ( $P_9/P_1$ ) once again depending on where the measurement is taken. This efficiency as expected is slightly higher than the efficiency obtained for the 2.0325° steering angle case. The theoretical limit for the 1.0161° steering angle case is about 42.1%. Calculating the diffraction efficiency at location P5 yields an efficiency of 36.73% ( $P_5/P_4$ ), which is much closer to the theoretical limit than the diffraction efficiency of ~26% calculated from P9 and P4. The reason for the discrepancy between the overall efficiency of the design and efficiency calculated at P5 is the use of an iris to isolate the first order of the beam from the zeroth order.

### 3.2.1 Discussions

The overall experimental diffraction efficiency was ~18% and ~25% for the  $2.0325^\circ$  and  $1.0161^\circ$  steering angles, respectively, while the theoretical limits for both angles were ~25% and ~42%. Reflection, absorption, and scattering losses in the chain of optics as well as the assumption that there is a non-perfect calibration of the SLM phase curve accounted for these discrepancies in the efficiency of the design. When comparing both the theoretical and experimental diffraction efficiencies of this proposed Tx/Rx switch design with the theoretical limit of the traditional Tx/Rx switch, a significant increase in diffraction efficiency is observed. The theoretical limit for the traditional Tx/Rx switch, which was achieved with a circular polarized beam illuminating a SLM in conjunction with a polarization beam splitter, is about 7%. This limit is obtained by considering that both the transmission and receiving paths of the PBS will each introduce a power loss of 50%, thus allowing for a maximum achievable efficiency of 25%. When multiplying this maximum efficiency by the ideal first order diffraction efficiency of 40.5% for the maximum steering angle and the maximum usable area of 69.6% of the SLM, the highest possible efficiency for this traditional Tx/Rx switch design without a Faraday rotator is ~7% for the maximum steering angle. For the  $1.0161^\circ$  steering angle case, the theoretical limit for the traditional design is about 14%. As a result, the goal of obtaining higher efficiency is verified for both steering angles.

In terms of the addition of the Faraday rotator in the Tx/Rx switch, it has been observed through the steering angle experiment that this device allows for a beam at about  $\pm 2^\circ$  degree angle to pass through without being cut-off by the housing of the large magnet,

which is the limiting factor with this device. Furthermore, the imaging quality of a target should not be affected by this large aperture Faraday rotator since the actual terbium gallium garnet (TGG) crystal located within the housing of the magnet [19] is relatively thin. A simple imaging experiment has been done in order to prove that this device does not introduce any aberrations in the imaging of a resolution target, which is done by measuring the modulation transfer function (MTF) of the image after the Faraday rotator. A separate report will be presented with the results.

As addressed in the previous chapter, the notion of flyback was originally thought to be a major player in affecting the efficiency of this design, especially at the maximum steering angle [8, 15]. However, according to a BNS technician, flyback does not wield as much affect over the efficiency due to the pixel pitch (15 $\mu$ m) being quite large in comparison to the typical liquid crystal gap (~2.5 $\mu$ m). Furthermore, flyback is much more of a problem on the linear arrays where the pixel pitch is 1.6 $\mu$ m since the pixel is significantly smaller than the LC gap. If flyback were a problem, then the overall diffraction efficiency [8] for this particular LC-SLM would be obtained from equation (3).

$$\eta_d = \eta_{11}\eta_{12} = \left( \text{sinc}^2 \left( \frac{1}{2^M} \right) \right) \left( \left( 1 - \frac{\Lambda_F}{\Lambda_g} \right)^2 \right)$$

### 3.3 Imaging Capabilities

As previously mentioned, the imaging quality should not be affected by this design. In order to demonstrate this, the mirror located after the quarter-wave plate, which is simulating a target, was positioned so that the beam illuminated the edge of this mirror.

Figure 3.5 shows the entire beam (left) and the mirror's edge (right) as viewed on the CCD camera.

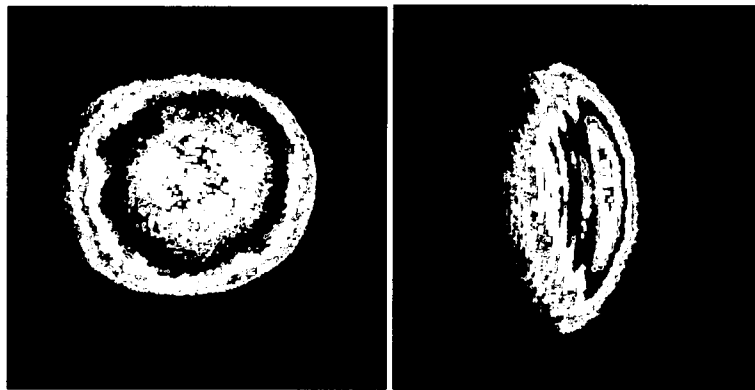


Figure 3.5 Image of entire beam (left) and of the edge of the mirror (right)

From these two images, the entire beam as shown on the left is indeed imaging the right edge of the mirror since the observer can clearly make out this edge in the rightmost picture. Of course, this simple exercise is only a verification of the preliminary imaging function. Further experimentation is required to fully test the imaging ability of this Tx/Rx switch design.



## CHAPTER IV: ELECTRONIC ELECTRO-OPTIC BEAM STEERING

### 4.1 Why Electronic Electro-Optic Beam Steering

The discussion thus far has focused on using a reflection type liquid crystal spatial light modulator for beam steering. This method of beam steering is viable; however, it does have a few noticeable disadvantages including slow scanning speed, small maximum steering angle, and somewhat low efficiency. In order to improve upon the speed and steering angle, a better method is required, which is where electronic electro-optic beam steering comes in. Electro-optic beam steering is based on the electro-optic (EO) effect, which is the change in the refractive index due to an applied electric field. Typically, the change in the refractive index is quite small; however, it has a significant impact on a wave propagating through a distance greater than a wavelength away. For example, a change in refractive index on the order of  $10^{-5}$  will result in a phase shift of  $2\pi$  for an optical wave transmitted a distance of  $10^5$  wavelengths [21].

A LC-SLM can be characterized as an electro-optic beam steering device that is based on molecule re-orientation under an applied electric field [21]. The elongated liquid crystal molecules undergo a change in orientation due to an applied electric field. Alignment of these molecules is completed at a relatively slow nonlinear response time ( $\sim$ ms), thus resulting in scanning speeds from a few tens of Hz to a few kHz. As for electronic electro-optic beam steering devices, they are based on the electronic polarization effect. This effect relates to how the electron cloud surrounding the nucleus of an atom/molecule

of the electro-optic material is deformed upon the application of an electric field. Such an electronic response is much faster ( $\sim$ fs), which results in a faster obtainable scanning speed (GHz) than that of the LC-SLM.

There are many different ways to achieve beam steering using the electronic EO effect. The easiest way to accomplish this is by using a prism made of electro-optic material. With such a prism, the deflection angle can be adjusted based on the refractive index being controlled by an applied field [20]. In particular, a prism can be utilized as a scanner since its beam bending capability is controllable. The change of the deflection angle,  $\Delta\theta$ , is given by [21]

$$\Delta\theta = \alpha\Delta n = -\frac{1}{2}\alpha rn^3 E = -\frac{1}{2}\alpha rn^3 \frac{V}{d}, \quad (22)$$

$$r = -\frac{2a_1}{n^3} \quad (23)$$

where  $\alpha$ ,  $\Delta n$ ,  $r$ ,  $n$ ,  $E$ ,  $V$ , and  $d$  represent the apex angle of the prism, the change of the refractive index, electro-optic coefficient, the refractive index, applied electric field, applied voltage, and the prism width. From equation (22), the change of the deflection angle,  $\Delta\theta$ , is varied proportionally in accordance with changing the applied voltage,  $V$ , thus allowing for the incoming light to be scanned. The electro-optic coefficient as shown in equation (23) depends on the polarization of the light as well as the direction of the applied electric field,  $E$  [21]. However, this method requires the use of bulk EO crystals, which limit the steering angle to less than a few degrees and lead to a slow response speed because the alignment of the crystal molecules is a relatively slow nonlinear process.

In this chapter, I will discuss a beam steering concept that utilizes a lateral beam shifter based on the electronic EO effect (illustrated in Fig. 4.1). When this beam shifter is placed at the focal plane of a parabolic mirror, the focal shift will lead to a steering angle upon the reflection off the parabolic mirror. With a reasonable lateral shift and a carefully chosen parabolic mirror, very large steering angles can be obtained. The translation of the mirror affects the beam size at the output and the divergence angle. The angle-aperture products that are feasible are again based on the Lagrange invariant, which states the number of resolvable points that can be steered to [6]. In order to study the performance of a parabolic mirror, the beam optics must first be developed, which allows for the calculation of the steering angle and analysis of the Gaussian beam quality. Upon completing this study, the next step is to introduce a lateral shifter based on the Goos-Hänchen effect as a means to electro-optically shift the beam on the parabolic mirror. Overall, a fast and efficient electro-optic beam steering method that allows for a relatively large steering angle will result.

#### 4.2 Gaussian Beam Optics of Parabolic Mirror

As previously mentioned, a Goos-Hänchen shifter, which will be explained in greater detail in the next section, utilizes the electro-optic effect in order to provide a continuous lateral shift of a Gaussian beam on the parabolic mirror. Because of this shift, the parabolic mirror is able to steer the beam. A parabolic mirror was chosen instead of a lens for two main reasons. The first reason is that the aberrations caused by the mirror are not as severe as those caused by a lens. Secondly, the steering angle is larger for a parabolic mirror. For such a reflection system, a change in the incident angle leads to

double that amount of the steering angle; whereas, for a refraction system, which deals with using a lens, the change in the incident angle leads to less of a change in the steering angle. Figure 4.1 shows a block diagram representation of this architecture.

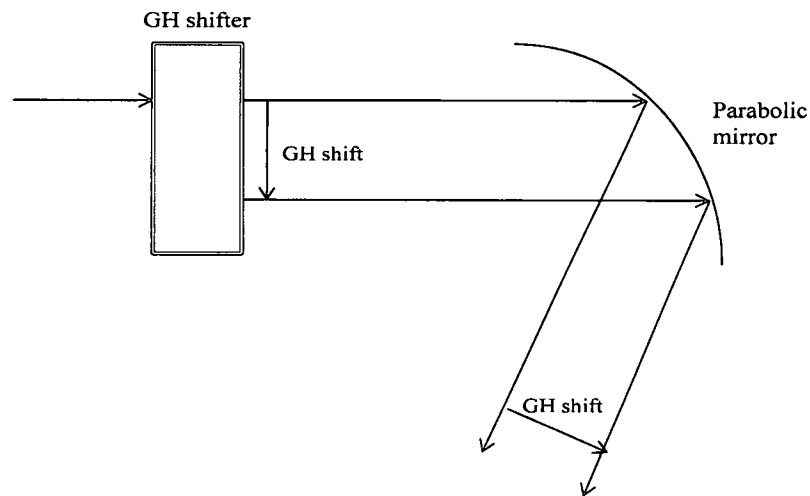


Figure 4.1 Block diagram representation for EO beam steering

From this figure, a shift in the lateral position of the beam occurs when an electric field is applied to the Goos-Hänchen shifter. A more detailed illustration and description of this Goos-Hänchen shifter will be presented in the next section. The main focus of this section is the performance of the parabolic mirror. Typically, laser beams are fundamentally Gaussian; therefore, the study of the performance of a parabolic mirror requires the use of Gaussian optics. Figure 4.2 shows an illustration of an incident beam reflecting off a parabolic surface.

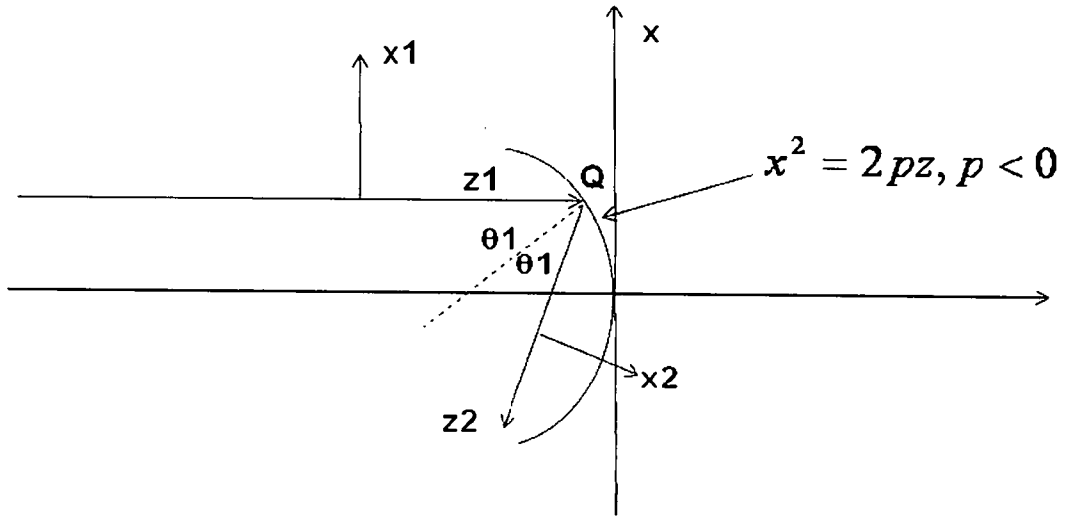


Figure 4.2 Reflection of a beam on a parabolic surface

This figure assists in deriving an ABCD matrix representation for both the reflection and refraction of Gaussian beams at a parabolic surface, which falls under the category of Gaussian optics [22]. For the purpose of this discussion, an abbreviated version of the derivation will be presented here with the full derivation available in [22]. Also, only the x-z coordinate system will be used.

As shown in Figure 4.2, the parabolic surface is represented by  $x^2 = 2pz$  where  $p$  is the focal parameter. By using the following relations [22],

$$x = x_1 - p \tan \theta_1 \quad (24)$$

$$z = z_1 + \frac{p \tan^2 \theta_1}{2} \quad (25)$$

the coordinates for point  $Q$  on the parabolic surface are found to be [22]

$$x_Q = -p \tan \theta_1 \quad (26)$$

$$z_Q = \frac{p \tan^2 \theta_1}{2} \quad (27)$$

When equations (24) and (25) are inserted into the equation for the representation of the parabolic surface, the relation becomes [22]

$$(x_1 - p \tan \theta_1)^2 = 2p \left( z_1 + \frac{p \tan \theta_1}{2} \right). \quad (28)$$

From this equation, the solution of  $z_1$  at the interface is given by [22]

$$z_1 = \frac{x_1^2}{2p} - x_1 \tan \theta_1. \quad (29)$$

After several equations and some substitutions, the phase of the incident wave at the interface can be expressed as [22]

$$\Phi_1(x_1, z_1) = kz_1 + \frac{kx_1^2}{2q_1} = k \left( \frac{x_1^2}{2p} - x_1 \tan \theta_1 \right) + \frac{kx_1^2}{2q_1}, \quad (30)$$

where  $q_1$  is the beam parameter of the incident Gaussian beam. For the reflected beam, the following coordinate transformations are used [22]

$$\begin{pmatrix} x_2 \\ y_2 \end{pmatrix} = \begin{pmatrix} \cos(\pi - 2\theta_1) & \sin(\pi - 2\theta_1) \\ -\sin(\pi - 2\theta_1) & \cos(\pi - 2\theta_1) \end{pmatrix} \begin{pmatrix} x_1 \\ y_1 \end{pmatrix} \quad (31)$$

in order to express the phase of the reflected beam at the interface, in terms of the  $(x_1, z_1)$  system, as [22]

$$\Phi_2(x_1, z_1) = \frac{kx_1^2}{2} \left( \frac{1}{q_2} - \frac{\cos 2\theta_1}{p} \right) + Cx_1 + \text{other terms}, \quad (32)$$

where  $q_2$  is the beam parameter of the reflected Gaussian beam. By setting equation (30) equal to (32), the following relation is obtained [22]

$$\frac{1}{q_2} - \frac{\cos 2\theta_1}{p} = \frac{1}{q_1} + \frac{1}{p}, \quad (33)$$

which can be simplified to

$$\frac{1}{q_2} = \frac{1}{q_1} + \frac{2 \cos^2 \theta_1}{p} \quad (34)$$

through the use of the trigonometric identity

$$\cos 2\theta_1 = 2 \cos^2 \theta_1 - 1.$$

Finally, using the beam parameters of the Gaussian beam, the following equations can be obtained

$$\frac{1}{q_1} = \frac{1}{R_1} - j \frac{\lambda_0}{\pi w_1^2} \quad (35)$$

$$\frac{1}{q_2} = \frac{1}{R_2} - j \frac{\lambda_0}{\pi w_2^2}. \quad (36)$$

Inserting equations (35) and (36) into equation (34) with  $w_1 = w_2$ , a relationship between the two radii of curvature,  $R_1$  and  $R_2$ , is derived as

$$\frac{1}{R_2} = \frac{1}{R_1} + \frac{2 \cos^2 \theta_1}{p}. \quad (37)$$

This equation allows us to connect the incident Gaussian and output Gaussian beams upon the reflection off a parabolic mirror.

For a Gaussian beam, if a surface is located at the beam waist, then  $R = \infty$ , which relates to a planar wave front with  $z = 0$ . As a result, equation (35) can be written as

$$q_0 = j \frac{\pi w_0^2}{\lambda_0}, \quad (38)$$

which gives the general relation

$$q(z) = z + j \frac{\pi w_0^2}{\lambda_0}. \quad (39)$$

From this relation, the Rayleigh range,  $z_0$ , is represented by

$$z_0 = \frac{\pi w_0^2}{\lambda_0}. \quad (40)$$

Finally, the relationships for the beam radius,  $w(z)$ , radius of curvature,  $R(z)$ , and beam divergence are given by

$$w^2(z) = w_0^2 \left[ 1 + \left( \frac{z}{z_0} \right)^2 \right] \quad (41)$$

$$R(z) = z \left[ 1 + \left( \frac{z_0}{z} \right)^2 \right] \quad (42)$$

$$\delta\theta = \tan^{-1} \left( \frac{\lambda_0}{\pi w_0} \right) \cong \frac{\lambda_0}{\pi w_0}. \quad (43)$$

Several of these equations will be utilized in the following subsections, thus leading to the experimental verification of using a parabolic mirror for beam steering.

#### 4.2.1 Setting Parameters for Experiment

The notion of using a parabolic mirror for beam steering as previously discussed revolves around Gaussian optics. In this subsection, the focus is on presenting the math behind the parabolic mirror. This will allow for a Gaussian beam profile via MatLab to be obtained as well as the steering angle calculation to be verified experimentally in the subsections to follow. First, a schematic of the setup is shown in Figure 4.3 with a 30° offset parabolic mirror. Note that the illumination of the incident beam on the parabolic mirror is parallel to the optic axis, which is not shown in the schematic.



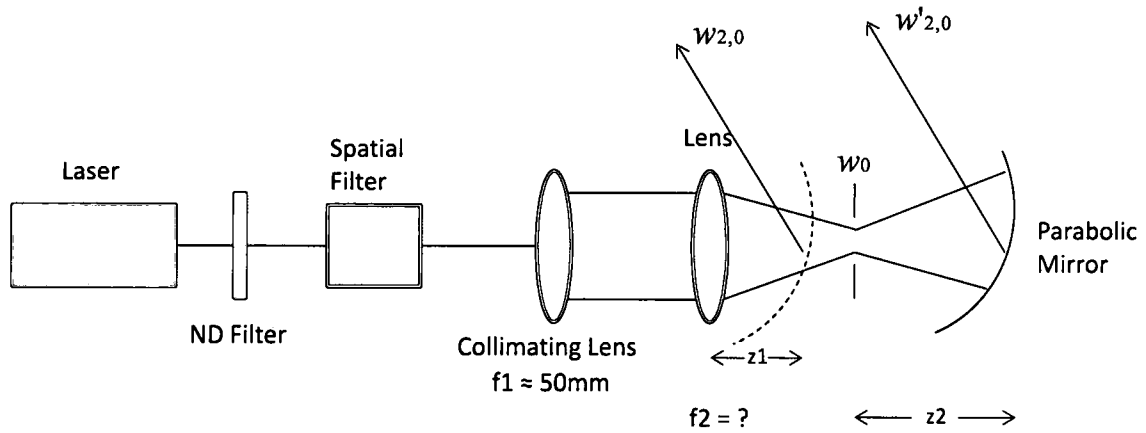


Figure 4.3 Schematic for beam steering with a 30° offset parabolic mirror

Using this schematic along with the parabolic mirror's parameters, the focal length of the second lens can be determined. The focal length,  $f$ , of the mirror is 50.8mm with an offset angle,  $\theta_1$ , of 30° or  $\pi/6$  radians. Start with equation (37) as derived earlier

$$\frac{1}{R_2} = \frac{1}{R_1} + \frac{2\cos^2 \theta_1}{p}$$

where  $p = -2f$ . In order to collimate the incident Gaussian beam, the left side goes to zero since  $R_2$  needs to be equal to infinity, which results in

$$\frac{1}{R} = -\frac{\cos^2 \theta_1}{f}. \quad (44a)$$

Setting (44a) equal to the equation (42) yields

$$R = z \left[ 1 + \left( \frac{z_0}{z} \right)^2 \right] = -\frac{f}{\cos^2 \theta_1}. \quad (44b)$$

Taking the derivative of the left portion above yields the following:

$$\frac{dR}{dz} = 1 + \frac{d}{dz} \left( \frac{z_0^2}{z} \right) = 1 - \frac{z_0^2}{z^2} = 0 \Rightarrow z = z_0.$$

By doing this, the distance,  $z$ , relating to the minimum value of  $R$  is obtained. This value is then put back into equation (44b) in order to determine what the Rayleigh range,  $z_0$ , is

$$R_{\min} = 2z_0 \leq \frac{f}{\cos^2 \theta_1} . \quad (45)$$

Note that (44a) is the condition for the incident Gaussian beam to be collimated. In other words, the radius of curvature,  $R$ , of the incident Gaussian beam needs to be equal to the value in (44a) in order to have a chance to be collimated by the parabolic mirror. For a Gaussian beam, the minimum  $R$  is given by its Rayleigh range,  $R_{\min} = 2z_0$ . Therefore, in order for the Gaussian beam to have a chance to be collimated,  $R_{\min}$  must be less than the right side of (44a). If  $R_{\min}$  is exactly equal, then the incident Gaussian beam waist needs to be right at the mirror. On the other hand, if it is less, then there will be two possible positions for the Gaussian beam to have the necessary radius of curvature in order to satisfy (44a). Expression (45) yields  $z_0 \leq 33.865\text{mm}$ . When this relation is inserted into equation (40), the beam waist,  $w_0$ , can be found as follows:

$$z_0 = \frac{\pi w_0^2}{\lambda_0} \leq 33.865\text{mm}$$

$$w_0 \leq \sqrt{\frac{z_0 \lambda_0}{\pi}} = 82.60\mu\text{m}$$

$$w_0 \leq 82.60\mu\text{m}$$

where the wavelength is  $\sim 633\text{nm}$ . Finally, the focal length of the second lens can be calculated from

$$w_0 = f_2(\delta\theta) \quad (46)$$

where  $\delta\theta$  is the divergence angle and is given by the paraxial approximation of equation (43)

$$\delta\theta = \frac{\lambda_0}{\pi w_{10}} = \frac{\lambda_0}{\pi \left(\frac{d}{2}\right)} = \frac{2\lambda_0}{\pi d}. \quad (47)$$

Inserting the relation from (47) into (46) gives

$$f_2 \left( \frac{2\lambda_0}{\pi d} \right) \leq 82.6 \mu m$$

$$f_2 \leq 1024.86 mm$$

where the diameter of the beam,  $d$ , is 5mm. This gives the allowable range of the focal length for the second lens. In our case, the focal length is chosen to be  $f_2 = 500mm$ .

Due to the quadratic nature of equation (42), there will be two positions,  $z_1$  and  $z_2$ , that will give the right value of  $R_1$  to match the parabolic mirror curvature and get collimated after reflection. With the focal length of the second lens being fixed, the beam waist, the locations  $z_1$  and  $z_2$ , beam spot sizes at these two locations, and divergence angles for both possible locations for the parabolic mirror can be calculated. Using equation (46), the beam waist is found to be  $\sim 40.3 \mu m$ . With this value, the two distances can be calculated from (42)

$$R = z \left[ 1 + \left( \frac{z_0}{z} \right)^2 \right] = z \left[ 1 + \left( \frac{\pi w_0^2}{\lambda z} \right)^2 \right] = 67.73 mm,$$

thus yielding  $z_1 = 973.2 \mu m$  and  $z_2 = 66.76 mm$ . By utilizing the same relationship as in equation (40), these distances determine the beam radii,  $w_{2,0}$  and  $w'_{2,0}$ , to be  $14 \mu m$  and

116 $\mu$ m, respectively. Finally, the divergence angles,  $\delta\theta_{2,0}$  and  $\delta\theta'_{2,0}$ , are calculated to be 0.8246° and 0.09952°, respectively.

Based on the values that were obtained for both possible locations of the parabolic mirror, the location at a distance,  $z_2$ , from the second lens is where the parabolic mirror will be positioned for the experimental portion in order to minimize the divergence angle of the steered Gaussian beam output.

#### 4.2.2 Gaussian Beam Profile

Having the second lens with a focal length of 500mm in the setup, the parabolic mirror is positioned at about 566mm from this lens. A CCD camera was then positioned on a one meter long rail in order to record the beam at various distances from the mirror. Figure 4.4 shows the experimental setup for beam profiling.

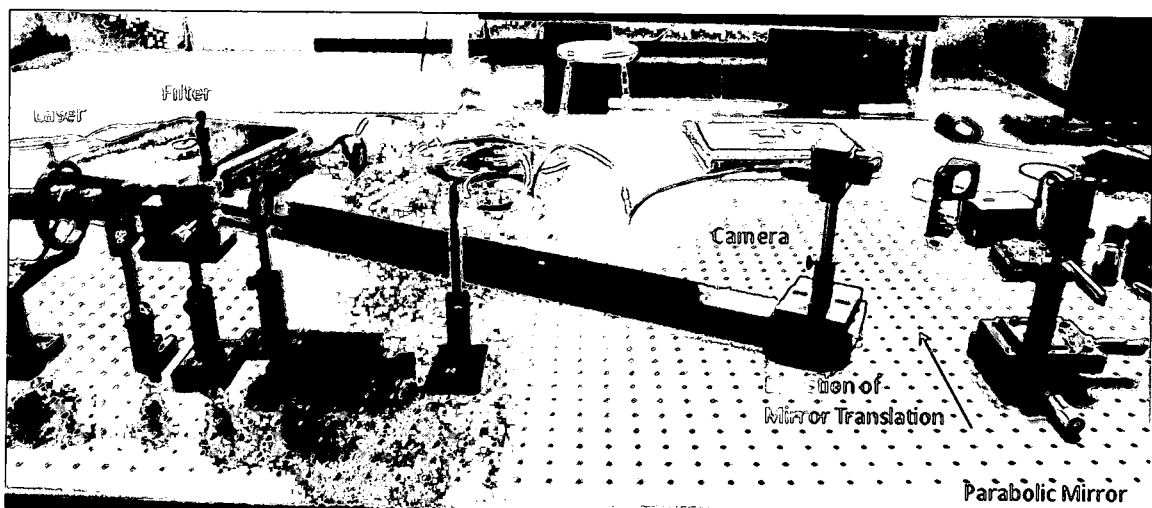


Figure 4.4 Experimental setup for beam profiling

From this figure, a HeNe laser ( $\sim 633\text{nm}$ ) is the source followed by a ND filter, which prevents saturation of the beam, a spatial filter, a collimating lens ( $f_1 \approx 50\text{mm}$ ), a 500mm lens, a  $30^\circ$  offset parabolic mirror (Edmund Optics) positioned on a one inch translation stage, and a CCD camera (Spiricon). There are also three ND filters on the camera itself.

The first step to obtaining a Gaussian beam profile of the setup was measuring the distance offset,  $z_{off}$ , which is the distance between the starting location of the camera and the mirror. This distance was found to be  $\sim 170\text{mm}$ . Next, the camera was moved in increments of four inches ( $101.6\text{mm}$ ). At each position including the starting location ( $z_{off}$ ), the beam width in both the  $x$  and  $y$  directions was recorded for 16 frames. For each direction, the measurements were summed together and then an average width was obtained. The average widths for both directions were summed and divided in half, thus giving the radius of the beam for that location. The beam area at each location was then plotted using MatLab. Figure 4.5 presents the beam profile. See Appendix B.1.1 for MatLab code.

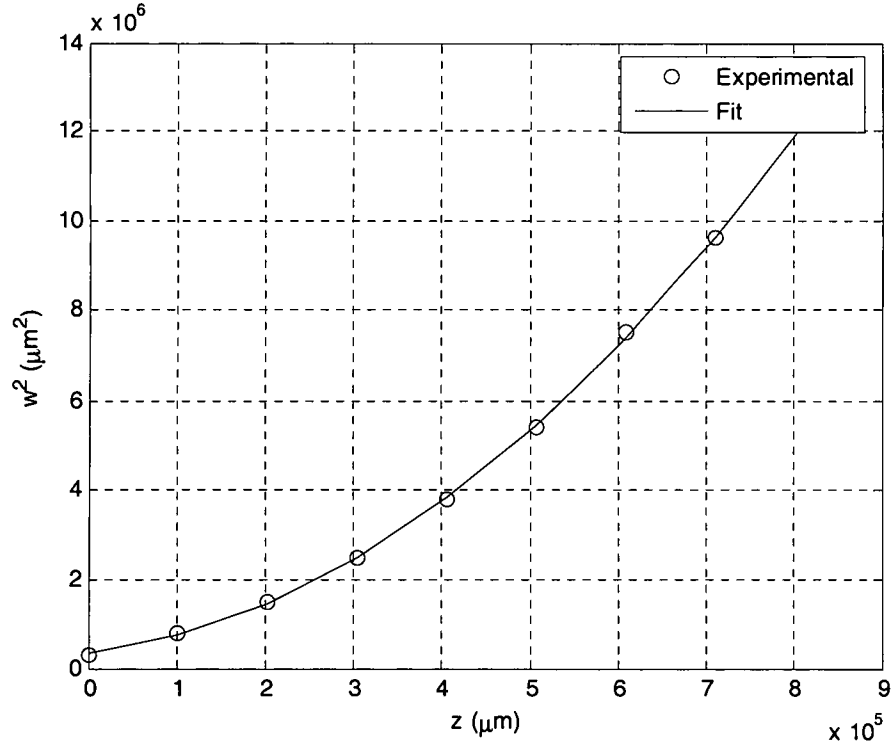


Figure 4.5 Gaussian beam profile of parabolic mirror

In this plot, the experimental data is fitted quite nicely against a polynomial curve fit. The algorithm for this curve fit was based on the equation for determining the beam radius

$$w^2 = w_0^2 \left[ 1 + \left( \frac{z}{z_0} \right)^2 \right] \quad (41)$$

where  $z$  is actually  $z + z_{off}$ . This equation is then expanded to give

$$w^2 = \frac{w_0^2}{z_0^2} z^2 + 2 \frac{w_0^2}{z_0^2} z_{off} z + \frac{w_0^2}{z_0^2} z_{off}^2 + w_0^2$$

which can simply be expressed as  $w^2 = az^2 + bz + c$  where

$$a = \frac{w_0^2}{z_0^2} = \frac{\lambda_0^2}{\pi w_0^2}$$

$$b = 2 \frac{w_0^2}{z_0^2} z_{off} = 2 \frac{\lambda_0^2}{\pi w_0^2} z_{off}$$

$$c = \frac{w_0^2}{z_0^2} z_{off}^2 + w_0^2 = \frac{\lambda_0^2}{\pi w_0^2} z_{off}^2 + w_0^2$$

Based on this algorithm, the beam waist was calculated to be  $\sim 52.42\mu\text{m}$  in MatLab, which is slightly greater than the value obtained in the previous section. In addition to the beam profile plot, two images were captured using the Spiricon software to illustrate the apparent change in size of the beam as the camera is taken from its initial position to its final position as presented in Figures 4.6 and 4.7.

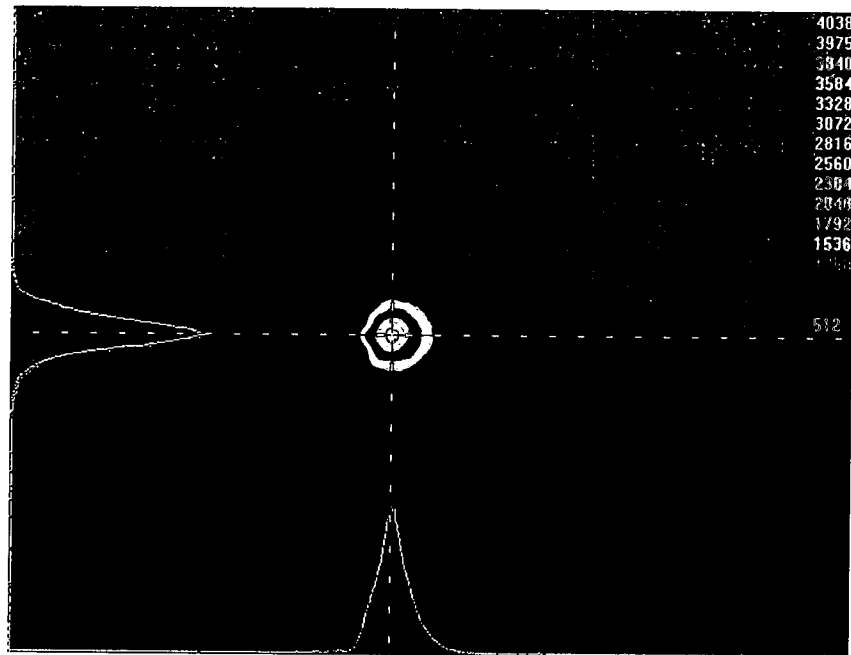


Figure 4.6 Image of beam at a distance,  $z_{off}$ , from the mirror

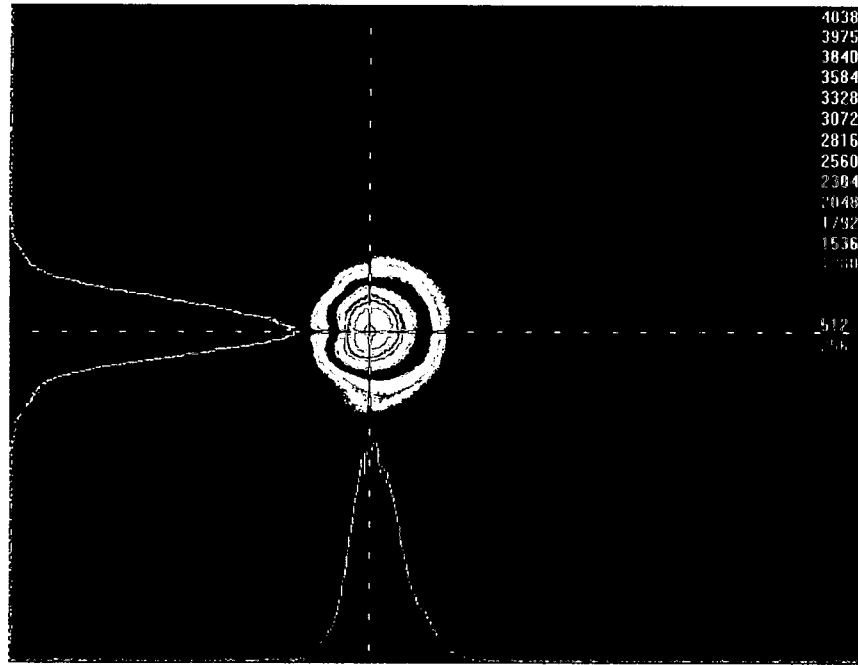


Figure 4.7 Image of beam at a distance of ~39 inches from the mirror

#### 4.2.3 Steering Angle Calculation

Keeping the same setup from Figure 4.4, a piece of paper was placed against a flat surface at a distance,  $D$ , of 1080mm from the mirror while the camera was at a distance,  $D_c$ , of 200mm from it. Along with these two measured parameters, the estimated distance that the beam's spot was from the mirror's edge,  $d$ , was found to be 15mm. Finally, the parabolic mirror, itself, has a focal length,  $f$ , of 50.8mm and a truncation or  $y$  offset,  $h$ , of 27.22mm. Using these parameters, the theoretical and experimental steering angles were able to be calculated. This procedure can be done using wide-angle decentered lenses as discussed in [23]. Figure 4.8 shows an illustration of an off-axis parabolic mirror [24].



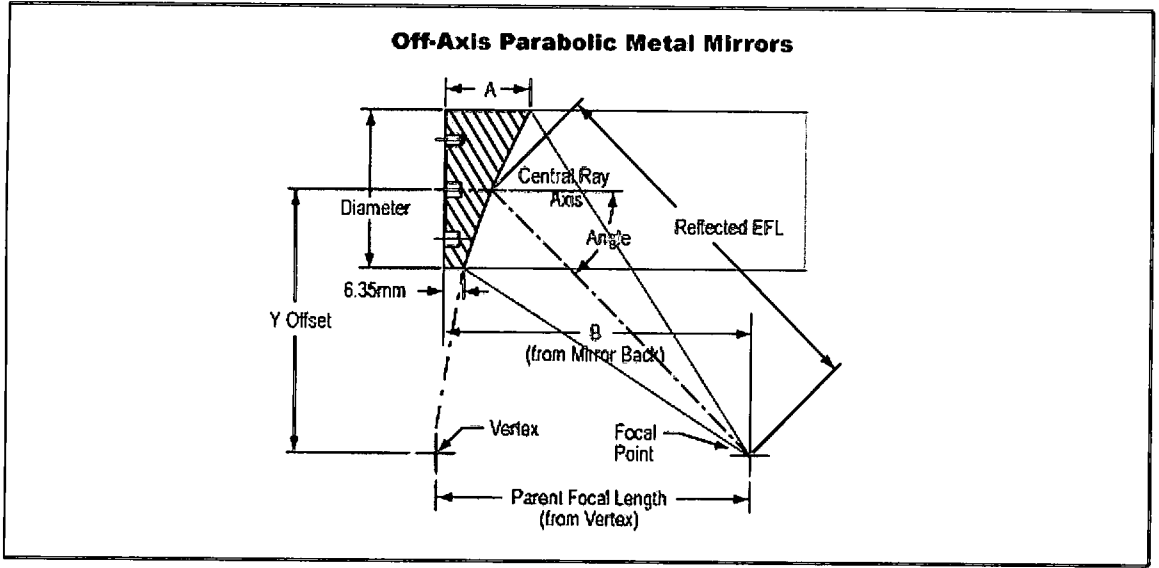


Figure 4.8 Illustration of an off-axis parabolic mirror

For the theoretical steering angle calculation, the relationship  $p = -2f$ , which is the radius of curvature of the mirror, was again considered in order to determine angles,  $\theta_1$  and  $\theta_2$ ,

$$\theta_1 = \tan^{-1} \left( \frac{h + d}{-p} \right) \quad (48)$$

$$\theta_2 = \tan^{-1} \left( \frac{h + d + t_m}{-p} \right) \quad (49)$$

where  $t_m$  represents the translation of the mirror by means of a translation stage. Taking these two angles, the steering angle can be calculated from

$$\Delta\theta = 2(\theta_2 - \theta_1) \left( \frac{180}{\pi} \right). \quad (50)$$

By translating the stage in increments of 1.27mm, which relates to half a tick mark on the translation stage, the theoretical steering angle was calculated for nine positions of the translation stage with the results presented in Table 4.1.

**Table 4.1 Theoretical steering angle calculation in terms of the mirror translation**

<b>Mirror Translation (mm)</b>	<b>Theoretical Steering Angle (°)</b>
1.27	1.2160
2.54	2.4211
3.81	3.6151
5.08	4.7980
6.35	5.9696
7.62	7.1299
8.89	8.2787
10.16	9.4161
11.43	10.5419

Experimentally, the steering angle can be determined from

$$\Delta\theta = \frac{t_{s,D}}{D} \left( \frac{180}{\pi} \right) \quad (51)$$

where  $t_{s,D}$  represents the translation of the spot (beam) on the piece of paper at a distance,  $D$ , of 1080mm from the mirror. Table 4.2 presents the calculated steering angle.

Table 4.2 Experimental steering angle calculation in terms of the translation of the spot at a distance of 1080mm

Mirror Translation (mm)	Translation of Spot (mm)	Experimental Steering Angle (°)
1.27	26	1.3793
2.54	53	2.8117
3.81	80	4.2441
5.08	107	5.6765
6.35	134	7.1089
7.62	160	8.4883
8.89	186	9.8676
10.16	213	11.3000
11.43	239	12.6793

Finally, one measurement showing the shift in the position of the beam on the camera was done in order to verify the experimental steering angle calculation. Unfortunately, only one measurement could be done due to the limited field of view of the camera. The steering angle was calculated from

$$\Delta\theta = \frac{x_2 - x_1}{D_c} \left( \frac{180}{\pi} \right) \quad (52)$$

where  $x_1$ ,  $x_2$ , and  $D_c$  represent the position of the spot before translation, after translation, and the distance between the camera and the mirror, respectively. For a mirror translation of 1.27mm laterally, the beam's/spot's movement as recorded on the Spiricon software yielded a steering angle of 1.3576°, which is very close to the measurement calculated without the use of the Spiricon camera as seen in Table 4.2. For this calculation,  $D_c = 200\text{mm}$ ,  $x_1 = 1.047\text{mm}$ , and  $x_2 = 5.786\text{mm}$ .

When comparing the theory against the experiment, the theoretical steering angle calculations deviate a bit from those obtained experimentally. Such a discrepancy can be accounted to uncertainty through human error in measuring the various distances as well as any uncertainty in the translation stage. Figure 4.9 shows a plot of the theoretical and experimental steering angle values versus the mirror translation. See Appendix B.1.2 for MatLab code.

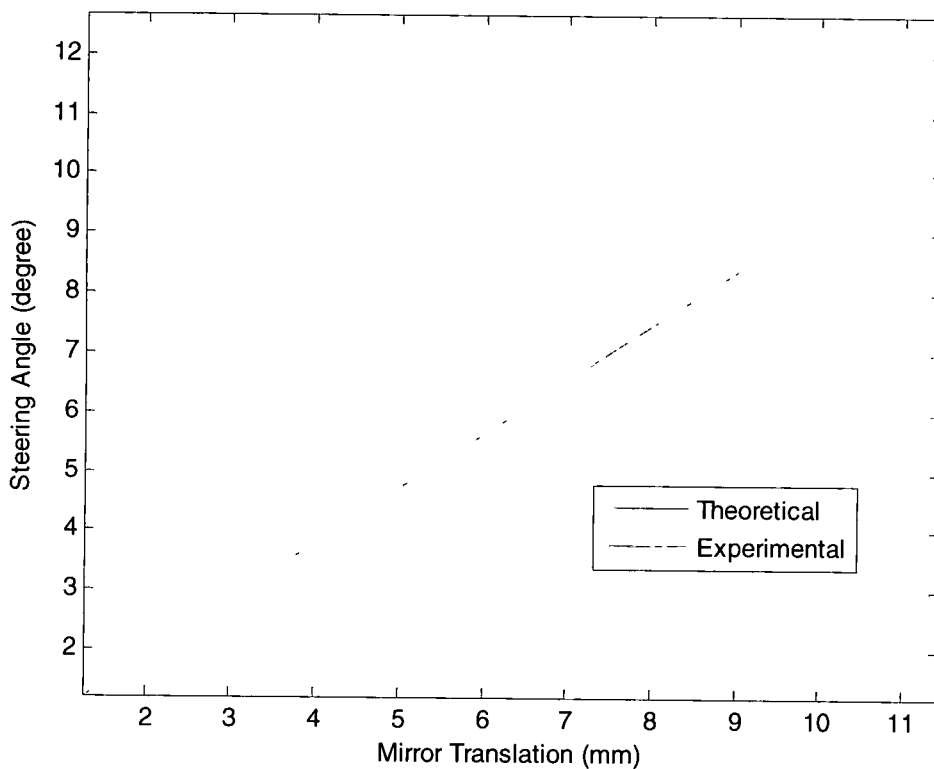


Figure 4.9 Plot of theoretical and experimental steering angles vs. mirror translation

### 4.3 Goos-Hänchen Shifter

In the previous section, the notion of using a parabolic mirror for beam steering has been discussed and experimentally verified. The mechanical translation of the mirror provided the necessary shift so that the parabolic mirror could steer the beam. However, in order

to achieve non-mechanical EO beam steering, a device that can provide this lateral shift of the incident beam at the focal plane of the parabolic mirror is necessary. In this section, I will introduce one such shifter that utilizes the Goos-Hänchen effect, namely a Goos-Hänchen shifter.

#### 4.3.1 Theory

This effect is characterized by a phase shift or lateral displacement of an optical wave undergoing total internal reflection [20, 25, 26]. Such a phenomenon contradicts the position where the beam should be located upon reflection as predicted by geometrical optics [25, 26]. In geometrical optics, total internal reflection occurs when the incident angle,  $\theta_i$ , is greater than the critical angle,  $\theta_c$ . The critical angle can be calculated from

$$\theta_c = \sin^{-1}\left(\frac{n_2}{n_1}\right) \quad (53)$$

where  $n_1$  represents the refractive index for an optically denser medium in comparison to  $n_2$  [27]. Figure 4.10 shows an illustration of the Goos-Hänchen effect where  $x_s$  represents the lateral or spatial displacement of an optical beam undergoing total internal reflection [28].

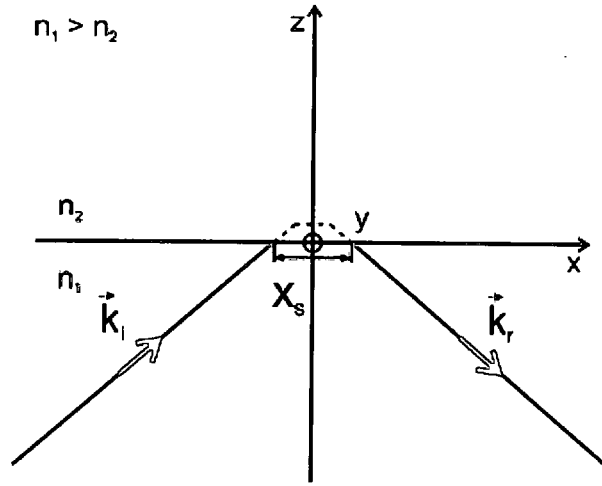


Figure 4.10 Illustration of Goos-Hänchen effect

From this figure, a beam is totally internally reflected at a planar interface between two dielectric media, thus resulting in the reflected beam being shifted by a distance,  $x_s$ , as mathematically represented by

$$x_s^E = \left( \frac{2}{k_1} \right) \frac{\tan \theta_c}{\sqrt{\sin^2 \theta_i - \sin^2 \theta_c}} \quad (54)$$

$$x_s^H = \frac{x_s^E}{\sin^2 \theta_c} \quad (55)$$

$$k_1 = \frac{2\pi n_1}{\lambda}$$

where the superscripts  $E$  and  $H$  represent the transverse electric (TE) and transverse magnetic (TM) vectors, respectively [27, 29].

Another example of the Goos-Hänchen shift can be seen in an optical waveguide or fiber as illustrated in Figure 4.11.

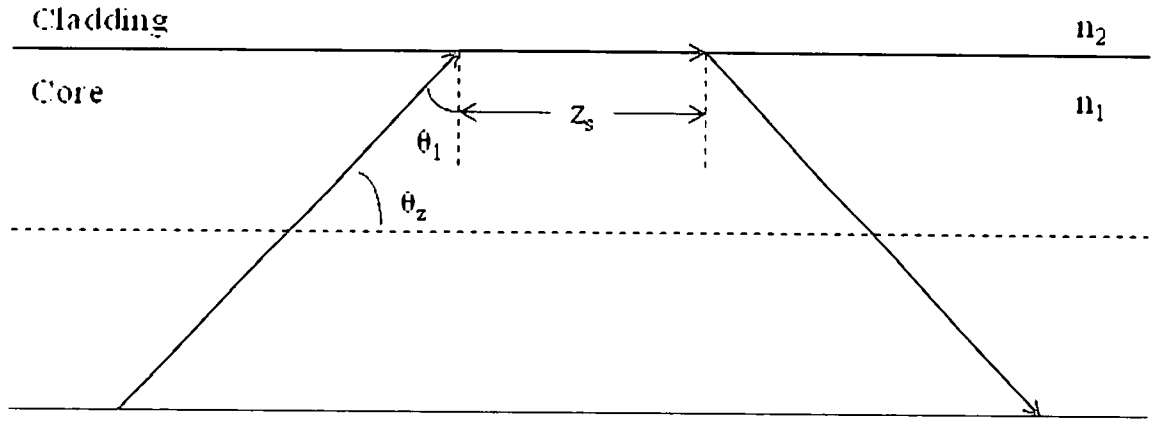


Figure 4.11 Illustration of Goos-Hänchen shift in a waveguide

Mathematically speaking, this lateral shift of  $z_s$ , which is known as the Goos-Hänchen shift, as shown in Figure 4.11 can be represented by [20]

$$z_s = -\left(\frac{\partial \phi}{\partial \beta}\right)_{\beta_1} \quad (56)$$

$$\beta_1 = k_1 \sin \theta_1 \quad (57)$$

$$\phi = -2 \frac{\sqrt{\theta_a^2 - \theta_z^2}}{\theta_z} \quad (58)$$

where  $\beta_1$  is the propagation constant parallel to the  $z$  axis and angles,  $\theta_z$  and  $\theta_a$ , are defined as

$$\theta_z = \frac{\pi}{2} - \theta_1 \quad (59)$$

$$\theta_a = \frac{\pi}{2} - \theta_c \quad (60)$$

Note that  $\theta_a$  is not shown in Figure 4.11 because it depends on the value of the critical angle, which will be less than  $\theta_1$  in this case; therefore,  $\theta_a > \theta_z$ . Equation (56) can then be written as

$$z_s = - \left( \frac{\partial \phi}{\partial \theta_z} \frac{\partial \theta_z}{\partial \beta} \right)_{\beta_1} \quad (61)$$

where

$$\frac{\partial \theta_z}{\partial \beta} = - \frac{1}{k \sin \theta_z} \quad (62)$$

Assuming that  $\theta_z$  and  $\theta_a$  are small angles, equation (61) can be differentiated to give

$$z_s \cong \frac{\lambda}{m_1 \theta_z} \frac{1}{\sqrt{\theta_a^2 - \theta_z^2}} \quad (63)$$

Experimentally, the Goos-Hänchen shift can be rather difficult to observe because it is “usually proportional to the penetration depth of the field with a scale of the wavelength” [25]. Hence we utilize a thin film resonator structure to enhance the Goos-Hänchen shift [30]. Figure 4.12 shows a more detailed illustration of this Goos-Hänchen shifter with thin film resonator structure.

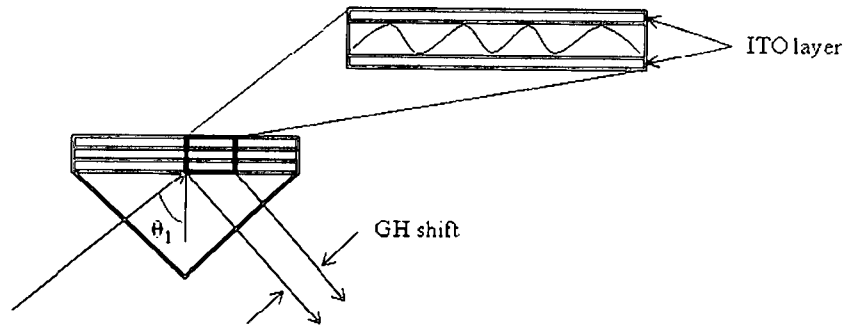


Figure 4.12 Illustration of Goos-Hänchen shifter

From this illustration, an EO polymer is deposited on a high refractive index prism and is in contact with air ( $n \approx 1$ ). Furthermore, this thin film resonator structure is a single layer



leaky mode structure with surrounding ITO (indium tin oxide) electrodes. Voltage is applied across these two ITO layers in order to shift/tune the resonance, thus resulting in a continuous shift of the beam. This shift in the prism can be expressed as

$$\Delta x_{GH} = \frac{\lambda}{2\pi} \frac{\partial \Phi}{\partial \theta_1}, \quad (64)$$

where  $\Phi$  represents the phase shift of the TE or TM reflected beam and  $\lambda$  is the wavelength of the incident beam. From this equation, the Goos-Hänchen shift is proportional to the slope  $\partial \Phi / \partial \theta_1$ ; therefore, a higher slope yields a lower angular resonance width [30]. As a result, resonances occurring in this thin film structure have led to the notion of the possible enhancement of the Goos-Hänchen shift. This concept is shown by using MatLab in the next section.

#### 4.3.2 Numerical Simulation

Having briefly discussed the theory behind the Goos-Hänchen shift, a numerical simulation using MatLab was done in order to see how the beam is shifted for both the transverse electric (TE) and transverse magnetic (TM) modes of the field. For this simulation, the thin film resonator structure is comprised of an EO polymer with an index and thickness of 1.49 and  $6\mu\text{m}$ , respectively. This polymer is surrounded by two ITO electrodes with a thickness of 50nm and indices of  $1.85 + 0.01i$  (top) and 1.85 (bottom) as shown in Figure 4.12. A wavelength of 633nm was used with a beam waist of 1 mm. These parameters are presented in the first two sections of the corresponding MatLab code given in Appendix B.1.3. The angular plane wave spectrum method is used to represent the incident Gaussian beam. The reflection coefficient of each of the plane wave components is calculated and the reflected beam profile is re-synthesized with these

reflection coefficients. The angle of incidence corresponding to the center of the angular plane wave spectrum,  $\theta_i$ , was selected to be  $53.5^\circ$ . The resulting plots for both the absolute and normalized beam profile versus the transverse distance are presented in Figure 4.13.

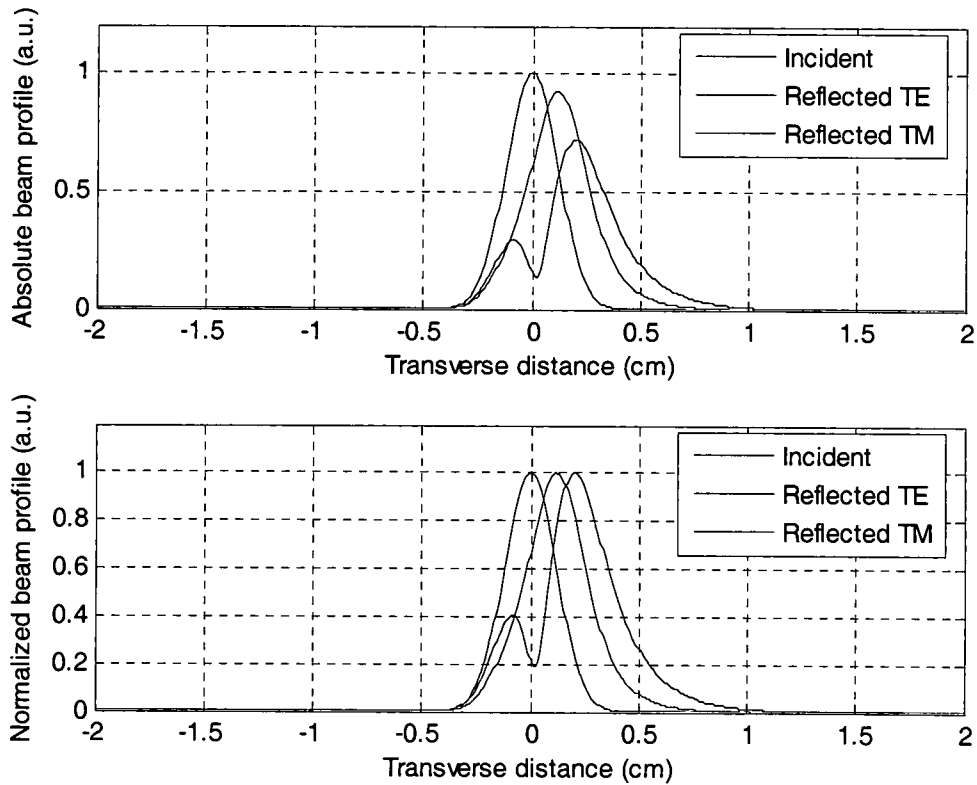


Figure 4.13 Plots showing both the absolute and normalized beam profile versus transverse distance

From these plots, a shift of 1.367mm and 1.953mm is observed for both the reflected TM and TE modes of the beam, respectively. Using equations (48) to (50), these shifts translate to steering angles of  $1.3085^\circ$  and  $1.8655^\circ$  if this shifter is combined with the parabolic mirror that we studied in the previous section. Obviously, both TE and TM polarization states experience Goos-Hänchen shifts; however, the TE case has a split due to a very sharp resonance. An extremely sharp resonance will give a larger shift;

however, it may also cause a split of the reflected Gaussian beam. When this occurs, that particular resonance cannot be used as a shifter because it destroys the Gaussian beam. As a result, a less sharp resonance at a different mode can be used. Figure 4.14 shows the resonances of various modes and the phase for both the TE and TM reflected beams plotted versus the incident angle of the incoming beam.

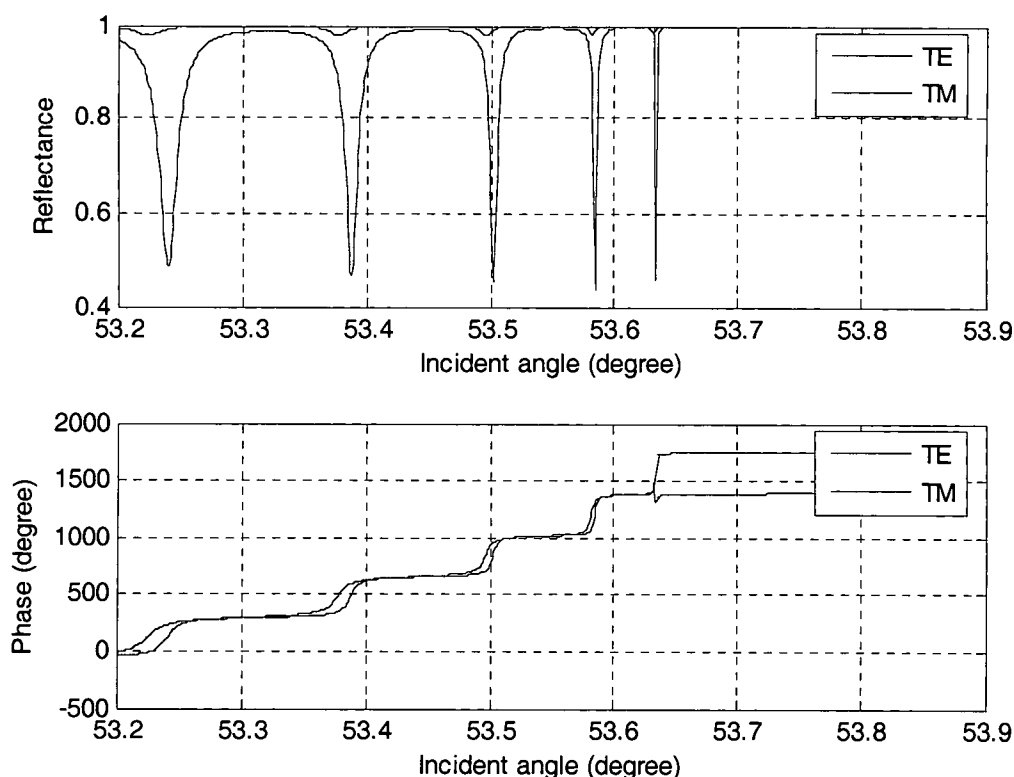


Figure 4.14 Plots showing the resonances of the various modes (top) and the phase (bottom) of the reflected beams versus the incident angle

For the beam profile calculations shown in Figure 4.13, the resonance at an incident angle of  $53.5^\circ$  was used. The resonance at an incident angle of about  $53.4^\circ$  could be used for the TE beam Goos-Hänchen shifter in order to avoid the beam split. In addition, we notice that the Goos-Hänchen shifter is also polarization dependent. Consequently, the large aperture Faraday rotator that was previously introduced can also be incorporated

into this electro-optic beam steering setup with the Goos-Hänchen shifter and parabolic mirror to provide an efficient Tx/Rx switch for electronic EO beam steering.

## CHAPTER V: CONCLUSIONS AND FUTURE WORK

An efficient transmit/receive (Tx/Rx) switch design for non-mechanical beam steering with a two-dimensional reflection type liquid crystal spatial light modulator (LC-SLM) being used in conjunction with a large aperture Faraday rotator is proposed and tested. In order for beam steering to be possible, a LC-SLM usually requires a linear polarized beam incident upon it. As a result, a polarization study was conducted using Jones calculus and a visual illustration. From this polarization study of the proposed Tx/Rx switch design, high throughput is expected along with good imaging quality. In comparison, a traditional Tx/Rx switch design utilizes a circularly polarized beam in conjunction with a polarization beam splitter, which results in a power loss of at least 50% from the beam splitter alone.

The polarization function of the Tx/Rx switch design has been confirmed with Jones matrix analysis. The steering capability of the LC-SLM was modeled both analytically and numerically and then simulated in MatLab. Analytically, the maximum diffraction efficiency in the first order was found to be 21.09%, which does not take into consideration the discrete phase levels of the SLM. When these discrete phase levels are considered, a numerical model simulation can be used to show that the first order diffraction efficiency for a maximum steering angle of  $\sim 2^\circ$  is 39.5%, which is very close to the calculated theoretical diffraction efficiency. Based on the manufacturer's specifications of the LC-SLM, the maximum diffraction efficiency in the zeroth order is

61.5%. By multiplying these two percentages together, the theoretical limit of the first order diffraction efficiency for the maximum steering angle is calculated to be ~25%.

An experimental verification of the proposed Tx/Rx switch design at an operational wavelength of  $1.064\mu\text{m}$  was done by conducting a power analysis for two different steering angles –  $1.0161^\circ$  and  $2.0325^\circ$ . First, the isolation capability of the Faraday rotator was tested by replacing the LC-SLM with a mirror in the setup. This resulted in a very good isolation ratio of 1.0633:1.0, which means that 1mW of power comes out for every 1.0633mW of power that goes into the Faraday rotator. Next, the overall diffraction efficiency of the zeroth order of the LC-SLM was measured to be 37.2%, which represents about a 47.75% power loss from the previous case with the mirror in the place of the LC-SLM.

Phase gratings have been displayed on the LC-SLM to provide about  $1^\circ$  and  $2^\circ$  steering angles. The theoretical limits for these two steering angles are ~42% and ~25%, respectively. Experimentally, the overall first order diffraction efficiency ( $P_9/P_1$ ) for both angles was found to be ~24% and ~18%, respectively. The reason for the discrepancy between the theoretical limit and the experimental result in the  $1.0161^\circ$  steering angle case is the use of an iris to isolate the first order of the beam from the zeroth order. Since the first order is so close to the zeroth order, it is difficult to entirely isolate the first order, thus resulting in some loss of power. Other contributors to the discrepancy between theory and experiment for both steering angles include scattering, reflection, and absorption losses in the chain of optics as well as the non-perfect

calibration of the SLM phase curve. If better quality optical components were to be used, higher efficiency should result. Also, the characterization of the Faraday rotator was addressed in terms of its allowable field of view and imaging quality in a separate report.

Finally, when the traditional Tx/Rx switch without a Faraday rotator is compared with the proposed design with a Faraday rotator, the experimental power efficiencies obtained for the proposed design are indeed higher than the traditional design's theoretical limits of 14% and 7% for  $1.0161^\circ$  and  $2.0325^\circ$  steering angles, respectively. In other words, higher efficiency is achieved for this proposed Tx/Rx switch design. Also, preliminary imaging was done on the mirror located after the quarter-wave plate in the setup. The edge of this mirror was successfully imaged onto the CCD camera. Future goals for this setup include making the design more compact and incorporating electro-optic beam steering into the setup by way of replacing the LC-SLM with a MEMS device, which is not polarization dependent.

Electronic electro-optic beam steering possesses several advantages over using a LC-SLM, such as a faster scanning speed, a larger steering angle, and higher efficiency. In particular, a parabolic mirror with an electro-optics focal plane shifter was discussed as a viable beam steering method. A Gaussian beam analysis upon the reflection off a parabolic mirror has been established. The theoretical and experimental steering angles were computed by translating the mirror. For the mirror translated by a lateral distance of 11.43mm, the theoretical and experimental steering angles were found to be  $\sim 10.5^\circ$  and  $\sim 12.6^\circ$ , respectively. The discrepancy between these two values can be attributed to

uncertainty through human error in measuring the various distances as well as any uncertainty present in the translation stage.

The electro-optic beam shifter based on the Goos-Hänchen effect has been analyzed. Currently, preliminary experimental work is being conducted for both an analog and a digital Tx/Rx switch design for beam steering utilizing the Goos-Hänchen shift. Future work includes combining the parabolic mirror with the Goos-Hänchen shifter to obtain a faster scanning speed, higher efficiency, and a larger steering angle.



## APPENDIX A

### A.1 MatLab Code for Generating the Analytical Model in Chapter 2

% analytical\_modeling\_1D\_discrete.m plots the analytical model of the beam at max  
% steering angle of 2.0325 deg  
% can be modified to include the beam being steered from 0.50803 deg to 2.0325 deg

%%

close all; clear all; clc;

% wavelength in microns

lambda = 1.064;

% pixel size/pitch in microns

pp = 15;

% fill factor

ff = 0.834;

% # of pixels in horizontal dimension

N = 512;

Kx = 2\*pi/pp;

% # of pixels in one period

M = input('Number of pixels in one period? ');

% Design aiming angle

theta = asin(lambda/(M\*pp))\*180/pi;

% constants

a = 1/abs(Kx);

b = ff\*a;

c = M\*a;

d = N\*a;

% wavenumber

k = (2\*pi)/lambda;

% define range of kx

kx = [-5\*Kx:(Kx/(4\*N)):5\*Kx];

%%

% define parameters for comparison purposes

p = kx./Kx;

m = kx-(round(p)\*Kx);

tau = 10^-8;

% define a 1 x size(kx) matrix of zeros

sinccomb1 = zeros(size(kx));

% finds where the comb function intersects with the sinc function, thus

% resulting in the necessary pixel pattern

```

sinccomb1(find(abs(m)<tau)) = (a*b)*sinc((ff*kx(find(abs(m)<tau)))/Kx);

%%%
% define parameters for comparison purposes
p1 = (M*kx)/Kx;
m1 = (M*kx)-(round(p1)*Kx);
tau = 10^-8;

% define a 1 x size(kx) matrix of zeros
sinccomb2 = zeros(size(kx));
% finds where the comb function intersects with the sinc function, thus
% resulting in the necessary blazed periodic phase
sinccomb2(find(abs(m1)<tau)) = c*sinc((M*(kx(find(abs(m1)<tau))-
(k*sin(theta*(pi/180)))))/Kx);

%%%
%convolution of pixel pattern and blazed grating
conv12 = convn(sinccomb1,sinccomb2);
% sinc function pertaining to mask of SLM
H = d*sinc(N*kx./Kx);
% convolution of conv12 and the mask of the SLM
conv1 = convn(conv12,H);

%%%
% define a 1 x size(kx) matrix of zeros
sinccomb3 = zeros(size(kx));
% finds where the comb function intersects with the difference of sinc functions, thus
% resulting in the necessary pixel pattern w/fill factor taken into account
sinccomb3(find(abs(m)<tau)) = a*((a*sinc(kx(find(abs(m)<tau)))/Kx)-
(b*sinc((ff*(kx(find(abs(m)<tau))))/Kx)));
% legend('pixels','gap func.','Location','Best')

%%%
% convolution of gap of each pixel (from fill factor) with the mask of the
% SLM
conv3 = convn(sinccomb3,H);
% define a delta function
delta = zeros(size(kx));
delta(find(abs(kx==0)))=1;
% convolve delta function with conv3
conv2 = convn(conv3,delta);

%%%
% define a larger range of kx
kxx = [-15*Kx:(Kx/(4*N)):15*Kx];

```

```

% map from k space to angle
thetax = asin(kxx./k)*180/pi;
% the two convolutions can be added together
SLM = conv1 + conv2;
% normalized intensity
nSLM = ((abs(SLM)).^2)/(sum((abs(SLM)).^2));
figure
plot(thetax,nSLM,'r')
axis tight
xlabel('Diffraction Angle (degrees)')
ylabel('Diffraction Efficiency')
legend('2.0325° steering angle','Location','Northeast')
axis([1.9 2.2 0 0.22])

```

## A.2 MatLab Code for Generating the Numerical Model in Chapter 2

### A.2.1 MatLab Code for Figure 2.6

```

% numerical_modeling_1D.m plots the numerical model of the beam at max. steering
% angle of 2.0325 deg

```

```

close all; clear all; clc;

% wavelength in microns
lambda = 1.064;
% pixel size/pitch in microns
pp = 15;
% fill factor
ff1 = 1;
ff2 = 0.834;
% # of pixels in one period
M = input('Number of pixels in one period? ');
% # of phase levels
lvl = 2^M;
% Design aiming angle
theta = asin(lambda/(lvl*pp))*180/pi;
% # of pixels in horizontal dimension
hp = 512;
% size of x dimension
X = 2*hp*pp;
% # of dots per pixel
N = 8*hp;
% spacing between each point
dx = X/(2*N);
% array for SLM mask

```

```

x = [(-N/2)*dx:dx:(N/2-1)*dx];

% map into k space
K = 2*pi/dx;
dk = K/N;
kx = [(-N/2)*dk:dk:(N/2-1)*dk];

% corresponding transmittance function
tx = exp(i*((2*pi)/lambda)*x*sin(theta*(pi/180)));

mask_SLM = zeros(size(x));
mask_SLM(find((x>=-X/4)&(x<=X/4)))=1;

% desired phase
phi = angle(tx);

% Discretized phase to be displayed on SLM
phi_SLM = [floor(phi/((2*pi)/lvl))]*(2*pi)/lvl;

% transmittance function for SLM
tx_SLM = exp(i*phi_SLM).*mask_SLM;

% Fourier transform of tx_SLM
txf_SLM = fftshift(fft2(tx_SLM))/N^2;

% Map k to angle
thetax = asin(kx/(2*pi/lambda))*180/pi;

% normalized intensity
txfn_SLM = (abs(txf_SLM).^2)/(sum(abs(txf_SLM).^2));

% diffraction efficiency x normalized intensity
SLM1 = txfn_SLM*(ff1^2);
SLM2 = txfn_SLM*(ff2^2);

plot(thetax,SLM1)
hold
plot(thetax,SLM2,'r')
xlabel('Diffraction Angle (degree)')
ylabel('Diffraction Efficiency')
legend('100% fill factor','83.4% fill factor','Location','Northeast')
axis([-15 15 0 0.45])

```

### A.2.2 MatLab Code for Figure 2.7

% numerical\_modeling\_1D\_discreteb.m plots the numerical model of the beam being  
% steered from 0.50803 deg to 2.0325 deg

close all; clear all; clc;

% wavelength in microns

lambda = 1.064;

% pixel size/pitch in microns

pp = 15;

% fill factor

ff1 = 1;

ff2 = 0.834;

% # of pixels in one period

M1 = input('Number of pixels in one period? ');

M2 = input('Number of pixels in one period? ');

M3 = input('Number of pixels in one period? ');

% # of phase levels

lv1 = 2^M1;

lv2 = 2^M2;

lv3 = 2^M3;

% Design aiming angles

theta1 = asin(lambda/(lv1\*pp))\*180/pi;

theta2 = asin(lambda/(lv2\*pp))\*180/pi;

theta3 = asin(lambda/(lv3\*pp))\*180/pi;

% # of pixels in horizontal dimension

hp = 512;

% size of x dimension

X = 2\*hp\*pp;

% # of dots per pixel

N = 8\*hp;

% spacing between each point

dx = X/(2\*N);

% array for SLM mask

x = [(-N/2)\*dx:dx:((N/2)-1)\*dx];

% map into k space

K = 2\*pi/dx;

dk = K/N;

kx = [(-N/2)\*dk:dk:((N/2)-1)\*dk];

% corresponding transmittance functions

tx1 = exp(i\*((2\*pi)/lambda)\*x\*sin(theta1\*(pi/180)));

tx2 = exp(i\*((2\*pi)/lambda)\*x\*sin(theta2\*(pi/180)));

tx3 = exp(i\*((2\*pi)/lambda)\*x\*sin(theta3\*(pi/180)));

```

mask_SLM = zeros(size(x));
mask_SLM(find((x>=-X/4)&(x<=X/4)))=1;

% desired phases
phi1 = angle(tx1);
phi2 = angle(tx2);
phi3 = angle(tx3);

% Discretized phases to be displayed on SLM
phi_SLM1 = [floor(phi1/((2*pi)/lv1))]*(2*pi)/lv1;
phi_SLM2 = [floor(phi2/((2*pi)/lv2))]*(2*pi)/lv2;
phi_SLM3 = [floor(phi3/((2*pi)/lv3))]*(2*pi)/lv3;

% transmittance functions for SLM
tx_SLM1 = exp(i*phi_SLM1).*mask_SLM;
tx_SLM2 = exp(i*phi_SLM2).*mask_SLM;
tx_SLM3 = exp(i*phi_SLM3).*mask_SLM;

% Fourier transform of tx_SLM1, tx_SLM2, and tx_SLM3
txf_SLM1 = fftshift(fft2(tx_SLM1))/N^2;
txf_SLM2 = fftshift(fft2(tx_SLM2))/N^2;
txf_SLM3 = fftshift(fft2(tx_SLM3))/N^2;

% Map k to angle
thetax = asin(kx/(2*pi/lambda))*180/pi;

% normalized intensities
txfn_SLM1 = (abs(txf_SLM1).^2)/(sum(abs(txf_SLM1).^2));
txfn_SLM2 = (abs(txf_SLM2).^2)/(sum(abs(txf_SLM2).^2));
txfn_SLM3 = (abs(txf_SLM3).^2)/(sum(abs(txf_SLM3).^2));

% diffraction efficiency x normalized intensity
SLM1a = txfn_SLM1*(ff1^2);
SLM1b = txfn_SLM1*(ff2^2);
SLM2a = txfn_SLM2*(ff1^2);
SLM2b = txfn_SLM2*(ff2^2);
SLM3a = txfn_SLM3*(ff1^2);
SLM3b = txfn_SLM3*(ff2^2);

plot(thetax,SLM1a)
hold
plot(thetax,SLM1b,'r')
plot(thetax,SLM2a,'k')
plot(thetax,SLM2b,'g')
plot(thetax,SLM3a,'m')

```

```
plot(thetax,SLM3b,'c')
xlabel('Diffraction Angle (degree)')
ylabel('Diffraction Efficiency')
legend('2.0325°, 100% ff','2.0325°, 83,4% ff','1.0161°, 100% ff','1.0161°, 83,4% ff','0.50803°, 100% ff','0.50803°, 83,4% ff','Location','Northeast')
axis([-15 15 0 1])
```

## APPENDIX B

### B.1 MatLab Code for Generating Figures in Chapter 4

#### B.1.1 MatLab Code for Figure 4.5

% Beam\_Profile.m plots the beam profile of the parabolic mirror

close all; clear all; clc;

% run 1

% width x1 & width y1 in microns

wx1 = [561.0 561.6 561.3 561.5 561.2 561.3 560.8 561.2 561.6 561.2 561.6 561.2 561.2  
561.3 561.6 560.7];

wy1 = [538.5 538.5 538.0 538.4 538.2 538.3 537.9 538.2 538.3 538.9 538.3 538.3 537.9  
537.9 538.0 537.8];

wx1 = sum(wx1)/16;

wy1 = sum(wy1)/16;

% determine beam radius

w1 = (wx1+wy1)/2;

% run 2

% width x2 & width y2 in microns

wx2 = [890.4 890.1 890.0 890.0 890.3 890.6 890.4 890.9 890.7 890.6 890.2 890.7 890.8  
891.0 891.1 891.3];

wy2 = [888.4 888.5 888.5 888.3 888.6 888.4 888.7 888.7 888.8 888.7 888.8 888.7 888.9  
888.9 889.0 889.2];

wx2 = sum(wx2)/16;

wy2 = sum(wy2)/16;

% determine beam radius

w2 = (wx2+wy2)/2;

% run 3

% width x3 & width y3 in microns

wx3 = [1212 1212 1212 1212 1212 1212 1212 1213 1213 1213 1213 1213 1213 1213  
1213 1213];

wy3 = [1239 1239 1239 1239 1239 1240 1239 1240 1240 1240 1240 1241 1240 1240  
1240 1240];

wx3 = sum(wx3)/16;

wy3 = sum(wy3)/16;

% determine beam radius

w3 = (wx3+wy3)/2;

% run 4



```
% width x4 & width y4 in microns
wx4 = [1554 1554 1554 1554 1554 1554 1554 1553 1553 1553 1553 1553 1553 1553
1553 1553];
wy4 = [1598 1598 1598 1599 1598 1599 1598 1597 1597 1598 1598 1598 1597 1597
1597 1597];
wx4 = sum(wx4)/16;
wy4 = sum(wy4)/16;
% determine beam radius
w4 = (wx4+wy4)/2;
```

```
% run 5
% width x5 & width y5 in microns
wx5 = [1922 1923 1923 1922 1923 1922 1923 1922 1922 1922 1923 1922 1922 1922
1923 1922];
wy5 = [1963 1963 1963 1963 1963 1963 1963 1963 1964 1963 1963 1963 1963 1963
1963 1963];
wx5 = sum(wx5)/16;
wy5 = sum(wy5)/16;
% determine beam radius
w5 = (wx5+wy5)/2;
```

```
% run 6
% width x6 & width y6 in microns
wx6 = [2303 2303 2303 2302 2301 2302 2302 2302 2302 2301 2302 2300 2301 2300
2300 2300];
wy6 = [2352 2350 2350 2351 2349 2351 2351 2351 2350 2349 2350 2347 2349 2349
2347 2346];
wx6 = sum(wx6)/16;
wy6 = sum(wy6)/16;
% determine beam radius
w6 = (wx6+wy6)/2;
```

```
% run 7
% width x7 & width y7 in microns
wx7 = [2731 2732 2731 2731 2732 2732 2733 2735 2734 2734 2733 2733 2731 2733
2732 2732];
wy7 = [2740 2742 2738 2739 2741 2742 2744 2746 2746 2745 2744 2744 2738 2741
2740 2740];
wx7 = sum(wx7)/16;
wy7 = sum(wy7)/16;
% determine beam radius
w7 = (wx7+wy7)/2;
```

```
% run 8
% width x8 & width y8 in microns
```

```

wx8 = [3105 3103 3103 3103 3104 3105 3105 3103 3105 3104 3105 3106 3106 3105
3105 3104];
wy8 = [3106 3105 3106 3105 3106 3106 3105 3104 3106 3107 3105 3107 3109 3109
3108 3109];
wx8 = sum(wx8)/16;
wy8 = sum(wy8)/16;
% determine beam radius
w8 = (wx8+wy8)/2;

% run 9
% width x9 & width y9 in microns
wx9 = [3491 3492 3491 3492 3492 3492 3492 3492 3494 3491 3491 3492 3491 3492 3491
3492 3490];
wy9 = [3488 3488 3489 3489 3488 3489 3489 3489 3488 3488 3486 3488 3488 3487
3488 3487];
wx9 = sum(wx9)/16;
wy9 = sum(wy9)/16;
% determine beam radius
w9 = (wx9+wy9)/2;

%
w = [w1 w2 w3 w4 w5 w6 w7 w8 w9];
% distances between mirror and camera
z = 10^3*[0 101.6 203.2 304.8 406.4 508.0 609.6 711.2 812.8];%[um]
% wavelength in microns
lam = 0.633;
format long
% polynomial curve fit
p = polyfit(z,w.^2,2);

a = p(1);
% beam waist in microns
w0 = sqrt(lam^2/(pi^2*a))

b = p(2);
% offset distance in microns
zoff = b/a/2

c = p(3);
% Rayleigh range in microns
z0 = pi*(w0^2/lam)

plot(z,w.^2,'o')
hold
wm = a.*z.^2+b.*z+c %[um^2]
plot(z,wm,'g')

```

```

grid
xlabel('z (\mum)')
ylabel('w^2 (\mum^2)')
legend('Experimental','Fit')

```

### B.1.2 MatLab Code for Figure 4.9

```

% parabolic_steering_angle.m plots the theoretical and experimental steering angles
% versus the mirror translation

```

```

close all; clear all; clc;

```

```

% mirror translation (mm)
tm = 1.27:1.27:11.43;

```

```

% theoretical steering angle values
theory = [1.2160 2.4211 3.6151 4.7980 5.9696 7.1299 8.2787 9.4161 10.5419];
% experimental steering angle values
exp = [1.3793 2.8117 4.2441 5.6765 7.1089 8.4883 9.8676 11.3000 12.6793];

```

```

plot(tm,theory)
hold
plot(tm,exp,'r')
xlabel('Mirror Translation (mm)')
ylabel('Steering Angle (degree)')
legend('Theoretical','Experimental','Location','Best')
axis tight

```

### B.1.3 MatLab Code for Figures 4.13 and 4.14

```

% ghshift.m calculates the Goos-Hanchen shift of Gaussian beam upon reflection

```

```

% ghshift calculate the GH shift of Gaussian beam upon reflection

```

```

close all; clear all; clc;

```

```

% Setup of the problem

```

```

% Index of incident medium
n1=1.85;
filmpara.n1=n1;
% Index of second medium
n2=1;
filmpara.n2=n2;

```

```

% parameter for film, if any
filmpara.n=[1.85 1.49 1.85+i*0.01];
filmpara.d=[0.05 10 0.05];
% wavelength (in micron)
lambda=0.633/n1;
k=2*pi/lambda;
% Gaussian beam parameters
w0=1000;

% Rayleigh range
z0=pi*w0^2/lambda;
q0=j*z0;
% Incident angle
thetai=53.501*pi/180;

% 56.151
% 56.394
% 56.539 --> double split

% Distance of interface from beam waist
zi=0;

% Coordinate at interface (z1=0)
N=2^10;
L=100*w0;
deltax=L/N;
x1=((1:N)-N/2)*deltax;
x1=fftshift(x1);

x=cos(thetai)*x1;
z=sin(thetai)*x1+zi;
pz=-j*log(1+z/q0);
qz=z+q0;
% Compute field at interface
Ei=exp(-j*k*z).*exp(-j*(pz+k*(x.^2)/(2*qz)));
% Decompose into angular plane wave spectrum
% Create a frequency shift
Ei=Ei.*exp(j*k*sin(thetai)*x1);

Ek=fft(Ei); % Angular plane spectrum

% Create frequency coordinates
deltak1=2*pi/L;
k1=((1:N)-N/2)*deltak1;
% Shift the frequency coordinates

```

```

k2=k1+k*sin(thetai);
% Compute corresponding incident angles
theta=asin(k2/k);
costheta=cos(theta);
% Compute reflection coefficients of each angle
% TMM code will be called for known GH shifter structure
% Only compute those angles with  $|k_2| < k$ ; namely propagating orders
beta=(53.2:0.001:53.8)*pi/180;
for i=1:length(beta)
    fresnel=multilayer(filmpara,cos(beta(i)),lambda*n1);
    rs1(i)=fresnel.rs;
    rp1(i)=fresnel.rp;
end

for i=1:length(theta)
    fresnel=multilayer(filmpara,cos(theta(i)),lambda*n1);
    rs(i)=fresnel.rs;
    rp(i)=fresnel.rp;
end

% Reflected Gaussian beam field computation
rs=conj(rs);
rp=conj(rp);
Ekrs=Ek.*fftshift(rs);
Ers=fftshift(iff(Ekrs));

Ekrp=Ek.*fftshift(rp);
Erp=fftshift(iff(Ekrp));
% Display
figure
subplot(2,1,1)
plot((fftshift(x1))*(10^-4),abs(fftshift(Ei)))
grid
hold
plot((fftshift(x1))*(10^-4),abs(Ers),'r')
plot((fftshift(x1))*(10^-4),abs(Erp),'g')
xlabel('Transverse distance (cm)')
ylabel('Absolute beam profile (a.u.)')
legend('Incident','Reflected TE','Reflected TM')
axis([-20*w0*10^-4 20*w0*10^-4 0 1.2])

subplot(2,1,2)
plot((fftshift(x1))*(10^-4),abs(fftshift(Ei)))
grid
hold

```

```

plot((fftshift(x1))*(10^-4),abs(Ers)/max(abs(Ers)), 'r')
plot((fftshift(x1))*(10^-4),abs(Erp)/max(abs(Erp)), 'g')
xlabel('Transverse distance (cm)')
ylabel('Normalized beam profile (a.u.)')
legend('Incident','Reflected TE','Reflected TM')
axis([-20*w0*10^-4 20*w0*10^-4 0 1.2])

```

```

figure
subplot(2,1,1)
plot(beta*180/pi,abs(rs1).^2)
xlabel('Incident angle (degree)')
grid
hold
plot(beta*180/pi,abs(rp1).^2, 'r')
xlabel('Incident angle (degree)')
ylabel('Reflectance')
legend('TE','TM')
subplot(2,1,2)
plot(beta*180/pi,unwrap(angle(rs1))*180/pi)
xlabel('Incident angle (degree)')
ylabel('Phase (degree)')
grid
hold
plot(beta*180/pi,unwrap(angle(rp1))*180/pi, 'r')
xlabel('Incident angle (degree)')
ylabel('Phase (degree)')
legend('TE','TM')

```

## REFERENCES

- [1] Hällstig, Emil. "Nematic Liquid Crystal Spatial Light Modulators for Laser Beam Steering." Diss. Uppsala University, 2004, 13.
- [2] Boulder Nonlinear Systems, "XY Phase Series and XY PhaseFlat Series Spatial Light Modulators," User manual (Rev. 3.1), (2005): 1-2.
- [3] Goodman, Joseph W. Introduction to Fourier Optics. Englewood, Colorado: Roberts & Company Publishers, 2005, 186-7, 212-5.
- [4] Tholl, Hans Dieter. "Novel Laser Beam Steering Techniques." Proc. of SPIE 6397 (2006): 1-12.
- [5] Titus, Chuck. "Light Deflection." 19 April 2001. Liquid Crystal Institute at Kent State University. 25 April 2009 <[http://www.lci.kent.edu/boslab/projects/light\\_deflection/index.html#Technologies](http://www.lci.kent.edu/boslab/projects/light_deflection/index.html#Technologies)>.
- [6] McManamon, Paul F. et al. "A Review of Phased Array Steering for Narrow-Band Electrooptical Systems." Proc. of IEEE 97.6 (2009): 1078-81.
- [7] Watson, Edward A. "Analysis of beam steering with decentered microlens arrays." Optical Engineering 32.11 (1993): 2665.
- [8] Stockley, Jay and Steve Serati. "Advances in Liquid Crystal Beam Steering." Proc. of SPIE 5550 (2004).
- [9] Spatial Light Modulators: XY Phase Series. 2007. Boulder Nonlinear Systems, Inc. 9 March 2009 <<http://www.bnonlinear.com/products/XYphase/XYphase.htm>>.
- [10] Watson, Edward A., Donald T. Miller, and Paul F. McManamon. "Applications and requirements for nonmechanical beam steering in active electro-optic sensors." Proc. of SPIE 3633 (1999): 216-25.
- [11] Diffraction Gratings. 2008. Optometrics. 9 March 2009 <[http://www.optometrics.com/products\\_gratings.html](http://www.optometrics.com/products_gratings.html)>.
- [12] Goda, Matthew E. et al. "Spatial Light Modulators: Liquid-crystal SLMs benefit the study of atmospheric turbulence." 1 May 2006. Laser Focus World. 9 March 2009 <<http://www.laserfocusworld.com/articles/255505>>.
- [13] Beam Steering Using Liquid Crystals. 8 May 2001. Boulder Nonlinear Systems, Inc. 26 April 2009 <<http://www.bnonlinear.com/papers/LCBeamSteering.pdf>>.

- [14] Sizinger, S. and J. Jahns. Microoptics. Berlin: Wiley-VCH, 2003, 129-33.
- [15] McManamon, Paul F. et al. "Optical Phased Array Technology." Proc. of IEEE 84.2 (1996): 270-1.
- [16] Linnenberger, Anna, Steve Serati, and Jay Stockley. "Advances in Optical Phased Array Technology." Proc. of SPIE 6304 (2006): 1.
- [17] Wang, Xinghua. Optical Phased Array Technology for Beam Steering and Wavefront Control. 7 March 2003. Liquid Crystal Institute at Kent State University. 25 April 2009 <<http://www.lcd.kent.edu/lcd2004/Documents/1080843391.pdf>>.
- [18] Spatial Light Modulators: XY Phase Series Data Sheet. Oct. 2004. Boulder Nonlinear Systems, Inc. 9 March 2009 <<http://www.bnonlinear.com/products/XYphase/data/XYPhase.pdf>>.
- [19] EOT 1030 – 1080nm Faraday Isolators. Electro-Optics Technology, Inc. 30 May 2009 <[http://eotech.com/techsupport/faraday/userguide/1030\\_1080Fara/loverview.php](http://eotech.com/techsupport/faraday/userguide/1030_1080Fara/loverview.php)>.
- [20] Davis, Christopher C. Lasers and Electro-Optics: Fundamentals and Engineering. United Kingdom: Cambridge University Press, 2002, 397-9, 465-9, 495.
- [21] Saleh, Bahaa E. A. and Malvin Carl Teich. Fundamentals of Photonics. New York, Chichester, Brisbane, Toronto and Singapore: John Wiley & Sons, Inc., 1991, 195–203, 697-9, 705, 709-10.
- [22] Liu, Hongzhan et al. "ABCD matrix for reflection and refraction of Gaussian beams at the surface of a parabola of revolution." Applied Optics 44.23 (2005): 4809-12.
- [23] Gibson, Jennifer L. et al. "Wide-angle decentered lens beam steering for infrared countermeasures applications." Optical Engineering 43.10 (2004) 2312-21.
- [24] Off-Axis Parabolic Metal Mirrors. 2009. Edmund Optics. 25 June 2009 <<http://www.edmundoptics.com/onlinecatalog/displayproduct.cfm?productID=2307>>.
- [25] Wang, Yi et al. "Electric control of spatial beam position based on the Goos-Hänchen effect." Applied Physics Letters 93 (2008).
- [26] Tamir, T. and H. L. Bertoni. "Lateral Displacement of Optical Beams at Multilayered and Periodic Structures." JOSA 61.10 (1971): 1397.
- [27] Snyder, Allan W. and John D. Love. "Goos-Hänchen shift." Applied Optics 15.1 (1976): 236.
- [28] Evanescent Wave Spectroscopy Group. Jagiellonian University Institute of Physics. 7 May 2009 <<http://users.uj.edu.pl/~tkawalec/?dir=21&lang=en>>.



R002594463

[29] Emile, O. et al. "Measurement of the Nonlinear Goos-Hänchen Effect for Gaussian Optical Beams." Physical Review Letters 75.8 (1995): 1511.

[30] Kaiser, R. et al. "Resonances in a single thin dielectric layer: enhancement of the Goos-Hänchen shift." Pure Applied Optics 5 (1996): 891-6.